Precambrian Research
May 2023, Volume 388 Pages 106996 (18p.)
https://doi.org/10.1016/j.precamres.2023.106996
https://archimer.ifremer.fr/doc/00903/101528/

Sedimentology and geochemistry of basinal lithofacies in the Mesoarchean (2.93 Ga) Red Lake carbonate platform, northwest Ontario, Canada

Afroz M. [1, 2, *], Fralick P. W. [1], Lalonde Stefan [2]

[1] Department of Geology, Lakehead University, Thunder Bay, Ontario P7B 5E1, Canada
[2] CNRS-UMR6538 Laboratoire Geo-Ocean, Institut Universitaire Européen de la Mer, Université de Bretagne Occidentale, 29280 Plouzané, France

* Corresponding author : M. Afroz, email address : munira.afroz@univ-brest.fr

Abstract :

The > 200 m thick Red Lake carbonate platform of the 2.940-2.925 Ga Ball Assemblage (Red Lake Greenstone Belt, Superior Province, Canada) is the oldest known carbonate platform preserved on Earth. This study exam-ined surface outcrops and multiple industry cored drill holes comprising a diverse assemblage of chemical and siliciclastic sedimentary rocks of the deeper water lithofacies associated with the shallow water carbonates. The offshore lithologies, underlying, interlayered with, and overlying the mainly stromatolitic carbonates, consist of alternating packages of sandstone, siltstone, carbonaceous slate, pyritic carbonaceous slate, chert, and oxide facies iron formation (OFIF). These interlayer with carbonate in transitional slope environments, which consist in places of carbonate with magnetite laminae above slumped carbonate debris in iron formation and/or carbo-naceous slate. Chert and OFIF were deposited further offshore in a suboxic environment, with lithology dependent on concentrations of seawater Fe(II) and silicic acid. The iron sulfides were deposited in a reducing, anoxic, and organic-rich bottom water and muddy pore water environment not conducive to Fe hydroxide or chert precipitation. Carbonaceous mud was the background sediment, accumulating during intervals when the precipitation of chert, Fe hydroxides, or massive layers of Fe sulfides was inhibited. The interlayering of differing assemblages of chemical and siliciclastic sedimentary rocks indicates temporal and spatial fluctuations in the chemistry of local paleo-seawater and variable sedimentation rates on the margins of the Red Lake carbonate platform. Post-Archean Australian Shale (PAAS)-normalized rare earth element (REE) systematics of carbonate and OFIF show positive La and Gd anomalies, super-chondritic Y/Ho ratios, and depleted light rare earth ele-ments (LREEs) relative to heavy rare earth elements (HREEs), similar to modern seawater, while the positive Eu anomalies in the carbonate and OFIF samples reflect hydrothermally influenced Archean seawater. The chemical sedimentary rocks exhibit enrichment of redox-sensitive elements (i.e., Cr, Mo, V, and U) compared to their siliciclastic associates. This, combined with concentrations of MnO up to 6.3 wt% and positive Ce anomalies in the iron formation directly below the carbonate platform, all indicate the likely presence of some O2 ca 2.93 Ga.

Highlights

► Red Lake Greenstone Belt contains Earth's oldest known, thick, carbonate platform. ► Outcrops and multiple cored drill holes provide excellent stratigraphic control. ► Interlayering of lithofacies suggests short to long term relative sea level changes. ► Precipitation rates of all types of chemical sediments varied temporally. ► Archean seawater REE chemistry is similar in shallow and deep areas of the shelf.

Keywords : Archean sedimentology, Iron formation, Carbonate platform, Mesoarchean ocean geochemistry, Red Lake Greenstone Belt, Superior Province

62

63 **1. Introduction**

64 Archean carbonate platforms constitute a repository of information related to ancient
65 microbial life, paleoenvironments, biogeochemical cycling, and the aqueous and isotopic
66 geochemistry of the fluids in which these occurred (Kamber and Webb, 2001; Webb and
67 Kamber, 2000). Well-preserved Archean platformal carbonates are common in the Neoarchean
68 Era, however, they are rare in the Paleoarchean (Allwood et al., 2006; Grotzinger, 1989; Van
69 Kranendonk et al., 2003). Carbonate assemblages older than 3.0 Ga are generally highly
70 silicified, with little or no original carbonate conserved, tend to occur in thicknesses of ~10 m
71 (3.48 Ga Dresser and 3.43 Ga Strelley Pool Formations, Pilbara Craton; Allwood et al., 2006,
72 2010; Van Kranendonk, 2006; Van Kranendonk et al., 2003) up to 30 m (Kromberg Formation,
73 Onverwacht Group, Barberton Greenstone Belt; Lowe & Knauth, 1977), and juxtaposed deeper
74 water facies are rarely preserved. During the late Mesoarchean and throughout the Neoarchean,
75 carbonate platforms were present in significantly greater abundance and thickness, for example,
76 the ~500 m-thick Mosher Carbonate of the late Mesoarchean (2.83 – 2.78 Ga) Steep Rock Group
77 of northwestern Ontario, Canada (Fralick and Riding, 2015; Riding et al., 2014) and the ~ 2 km-
78 thick late Neoarchean (2.59 - 2.52 Ga) Campbellrand-Malmani carbonate platform of the Ghaap
79 Group, South Africa (Beukes, 1987; Kamber and Webb, 2001; Knoll and Beukes, 2009; Sumner,
80 1996; Sumner and Grotzinger, 1996). These are two of the most well-preserved and well-
81 documented ancient platforms where both shallow and deeper water facies are present and have
82 provided important insights regarding early platform sedimentation processes, biogeochemical
83 cycling, and the chemistry of the overlying water column (Eroglu et al., 2017; Fralick and
84 Riding, 2015; Fralick et al., 2008; Klein and Beukes, 1989).

However, the current literature is limited regarding the understanding of platform evolution between the Paleoarchean and Mesoarchean, with only two platforms in this timeframe reported. The Mesoarchean 2.96 Ga Chobeni Formation of the Pongola Supergroup, South Africa contains several carbonate successions that altogether reach ~50 meters thick, and are characterized by the presence of well-developed, 5 to 60 cm-scale, stromatolitic bioherms, along with ooids, peloids, and oncoids (Beukes and Lowe, 1989; Siahi et al., 2016). The depositional environment of the Chobeni Formation has been inferred from the association of coarse-grained clastic rocks, ooids, storm deposits, and abundance of clastic detritus in carbonates along with the microbialitic carbonate rocks and has been suggested to reflect deposition in a tide-dominated, clastic-carbonate, shallow marine environment (Beukes and Lowe, 1989; Mason and Von Brunn, 1977; Siahi et al., 2016). Importantly, deeper water facies of the Chobeni platform are not preserved, leaving open important questions surrounding water chemistry, biogeochemical cycling, and sedimentary processes occurring in Mesoarchean slope and offshore environments.

The second is a Mesoarchean carbonate platform in the Red Lake Greenstone Belt (RLGB), NW Ontario, Canada, which is the oldest known thick carbonate platform on Earth, deposited between 2.940 Ga and 2.925 Ga (Corfu and Wallace, 1986). This 450-meter-thick succession of sedimentary rock contains ~200 meters of stromatolitic dolostone and subordinate occurrences of limestone with the remainder consisting of various types of chemical sedimentary and siliciclastic rocks. The lateral transition from shallow water carbonates to offshore sandstones, carbonaceous slates, chert, and iron formation, as well as the arrangement of lithofacies in the deeper water successions, is captured in a number of cored drill holes and represents the only known place in the Mesoarchean where the relationship between shallow and

deep water chemical strata is preserved. These stratigraphically equivalent offshore lithofacies of the carbonate platform constitute a significant archive of Mesoarchean sedimentation processes and paleoseawater chemistry and provide valuable information on Mesoarchean offshore depositional environments.

A preliminary sedimentological study on the stromatolites and "Atikokania" present in the carbonate section of the Red Lake carbonate platform was conducted by Hofmann et al. (1985). Further, McIntyre and Fralick (2017) described the peritidal stromatolites through outcrop examination and mapping, but with lesser attention to deeper subtidal sedimentary rocks, which outcrop poorly. They suggested that peritidal depositional features dominate the carbonate platform top and are composed of dolomitic carbonate whereas the deep subtidal to upper slope lithofacies are composed of calcite, which in crystal fan mounds were probably deposited as aragonite. Although McIntyre and Fralick (2017) provided detailed descriptions and depositional interpretations for the stromatolites and other carbonates present in a variety of depositional environments, the geochemical data they provided (major element, trace element including REE, and C, O, and Sr isotopic compositions) were limited to a small sample set (n=30), and little stratigraphic context was available. The sedimentological study of McIntyre and Fralick (2017) was focused on only outcrops representing shallow water carbonates with hints of some deep water rocks from scant outcrops and limited sample analysis, and no detailed facies analysis was done for the deeper water sedimentary rocks.

The current study emphasizes the basinal lithofacies of the carbonate platform containing chemical and fine-grained siliciclastic rocks using cored drill hole data and correlative outcrop sections. The addition of drill hole core analysis provided a unique opportunity as the shallow-to-deep water lateral transition was observed directly in multiple drill hole cores and the

deep water lithofacies that poorly outcrop (e.g., black slate, sulfidic slate) are well-preserved in the cores. Importantly, these drill core permit stratigraphic context to be applied to both lithofacies sequence analysis and to the observed vertical and lateral changes in geochemistry to better understand the paleoenvironment. We logged approximately 3000 m of industry drill core through the carbonate platform at Red Lake, providing much needed stratigraphic constraint on the diverse lithofacies expressed at this important locality. Our current study includes 110 whole rock geochemical analyses (major elements, trace elements, and REE) to establish a geochemical framework to accompany the stratigraphy reported here. Moreover, this study evaluates for the first time paleo-redox conditions at the depositional sites using trace element enrichments, and further examines REE systematics to better understand the depositional paleoenvironment during the formation of the substantially thick Mesoarchean carbonate platform at Red Lake.

2. Geological Setting

The Red Lake carbonate platform lies in the Red Lake Greenstone Belt (RLGB) of the Uchi Subprovince in western Superior Province (Figure 1). Supracrustal rocks of Uchi Subprovince include Mesoarchean tholeiitic-komatiitic oceanic platform sequences to Neoarchean basaltic-andesitic-rhyolitic calc-alkalic and tholeiitic volcanic arc sequences, both with chemical and siliciclastic sedimentary rocks (Card and Ciesielski, 1986; Hollings et al., 1999). The Mesoarchean (3000 to 2800 Ma) strata of the RLGB include Balmer, Ball, Slate Bay, and Bruce Channel assemblages (Figure 1). The Ball assemblage lies in the western portion of the RLGB belt and comprises ultramafic and mafic flows intercalated with minor volcanic rocks of intermediate and felsic composition and sedimentary rocks including the carbonate platform (Corfu and Wallace, 1986; Hofmann et al., 1985; Hollings et al., 1999; Pirie, 1981; Sanborn-Barrie et al., 2001, 2000). The age of the platform is well constrained by U-Pb zircon dating of

rhyolitic lapilli tuff below the carbonates and a rhyolitic flow above the carbonates which places deposition from 2940 ± 2 Ma to 2925 ± 3 Ma (Corfu and Wallace, 1986). The Mesoarchean carbonate platform and associated strata is comprised of various chemical sedimentary rocks, i.e., chert, magnetite-rich iron formation, sulfidic iron formation/slate, dolomitic carbonate mostly with stromatolitic and domal features, and calcitic carbonate, as well as siliciclastic sediments, i.e., sandstone, carbonaceous slate, siltstone, and conglomerate (McIntyre and Fralick, 2017). This sub-vertically dipping, lower amphibolite facies (Corfu and Wallace, 1986; Thurston and Breaks, 1978), sedimentary package is overlain and underlain by mafic to ultramafic volcanic rocks.

3. Methodology

Rock samples were collected from different lithofacies present in numerous outcrop locations in the Red Lake area (Figure 1). Approximately 3000 m of core was described in detail and samples were taken generally every 2 meters for geochemical analysis, thin sectioning, slabbing, and/or polishing. A total of 110 samples were selected from chert, oxide facies iron formations, carbonaceous slate with and without sulfides, carbonates, siltstone, and sandstone. These were analyzed for whole rock major, minor, and trace elements using a Varian Vista Pro Radial inductively coupled plasma (ICP) atomic emission spectrometer (AES) and Perkin-Elmer Elan DRC-e quadrupole ICP mass spectrometer (MS) at the Lakehead University Instrumentation Laboratory. The samples were crushed using a tungsten carbide plate and mallet and powdered in an agate ring mill. In order to obtain a highly pure chemical sedimentary fraction from the oxide facies iron formations, these were further treated by a simple magnetic separation procedure that involved suspending the powder in ultrapure water in a clean Pyrex beaker and applying a neodymium bar magnet to the bottom to retain the magnetite-rich fraction;

177 the non-magnetic fraction was suspended in the ultra-pure water by hand agitation and drained to
178 waste; the process was repeated several times to until the ultrapure water showed no visual
179 evidence of suspended material. The magnetite-rich fraction was then air-dried and treated
180 similar to the untreated whole rock powders. Subsequently, 0.5 g of powdered samples were
181 digested using three treatments with concentrated nitric and hydrofluoric acid. The dilution for
182 ICP-AES analysis was 200 times and for ICP-MS 1000 times. A blank was added for every 10
183 samples and two standard reference materials (BHVO - 2, QLO - 1) and one in-house standard (8
184 - 44A) (Fralick and Riding, 2015) were run for approximately every 25 samples. The
185 geochemical data for the major, trace, and rare earth elements is tabulated in the supplementary
186 materials (Appendix I). The detailed analytical accuracy and related statistics against the
187 reference values of the standard materials are also reported in the supplementary materials
188 (Appendix II).

189 A total of 30 sulfidic slate and black slate samples were analyzed to determine the carbon
190 and sulfur contents in these rocks via a standard TCD detector on a CHNS [Cl] Elementar vario
191 EL analyzer at the Lakehead University Instrumentation Laboratory. Elemental mapping of
192 slabbed core and outcrop samples was conducted using a Bruker M4 Tornado high-resolution
193 micro-X-Ray-Fluorescence (μXRF) scanner at the European Institute for Marine Studies
194 (IUEM), France. Polished thin sections were examined with an Olympus DP-70 petrographic
195 microscope using plane-polarized light (PPL) and cross-polarized light (XPL), whereas carbon-
196 coated thin sections were examined under a Hitachi SU-70 Schottky field emission scanning
197 electron microscope (FE-SEM-EDX).

198 **4. Results and Interpretation**

199 **4.1. Lithofacies Associations and Sedimentology**

200 Stratigraphic relationships were established from the cores of the nine drill holes collared
201 in the central and western outcrop areas (Figure 2; for locations see Figure 1). These were
202 augmented by examination of abundant outcrops throughout the study area. The mainly
203 dolomitic shallow water carbonate succession that (McIntyre and Fralick (2017) described
204 consists of laterally linked domal stromatolites, isolated domal stromatolites, large low-relief
205 domes, laminated carbonate, and ribbon rock, as well as layers and domes composed of crystal
206 fans. This carbonate succession is underlain by, overlain by, and intercalates with the offshore
207 facies described here. Carbonate is present in the offshore as massive laminae and slump breccia
208 associated with oxide iron formation, chert, carbonaceous slate with or without disseminated and
209 layered pyrite, siltstone, and sandstone.

210 **Carbonate – Magnetite**

211 Carbonate associated with iron oxides consists of white, cm-scale, calcite layers
212 alternating with mm-scale, magnetite-rich laminae (Figures 3 and 4A). Layering is parallel,
213 straight to slightly wavy, displaying no evidence of current activity. Contacts are mostly sharp
214 with sparse magnetite in the carbonate layers, though some contacts grade upward from a more
215 diffuse mixture of magnetite and calcite to purer calcite (Figure 3B). Recrystallization of the
216 carbonate and iron oxides has destroyed primary structures and textures. Inequigranular, fine to
217 coarse crystalline calcite grains shows xenotopic fabric in thin section. Inside the magnetite
218 layers, recrystallized euhedral magnetite has carbonate present as a matrix, though the small
219 calcite crystals are probably secondary (Figure 3C). These successions are relatively devoid of
220 siliciclastics, though the magnetite layers tend to have higher amounts of Al, especially along
221 their contact with the calcite laminae. This facies is absent in the drill hole cores and is rare in
222 outcrops. However, on the northwest shoreline of Hall Bay (outcrop - 4 in Figure 1), this facies is

223 present underlying stromatolitic carbonate and overlying slumped carbonate (Figure 2 inset), and
224 can also be observed on the shore in the area immediately south of the oxide facies iron
225 formations that were sampled by rock saw to the WNW of Galena Island (outcrop -1 in Figure
226 1).

227 **Slumped Carbonate**

228 Slumped carbonate occurs in association with oxide facies iron formation and/or
229 siliciclastic sediments on the shoreline of Hall Bay (Outcrop - 4 in Figure 1 and Figure 2). It is
230 not present in the drill holes to the east of this location, which are dominated by shallow water
231 lithofacies and shales, chert and iron formation that were deposited in the previous shallow water
232 area during highstand intervals. Thus it, and associated interlayered calcite and magnetite, mark
233 the transition from the shallow shelf to the west and lithofacies deposited in deeper water to the
234 east.

235 It is comprised of mass-flows consisting of contorted, white to orange carbonate clasts
236 and broken layers, which differ in size and shape. The carbonate clasts and broken layers are
237 composed of calcite, hosted in fine-grained, dark gray to black mudstone, magnetite-rich iron
238 formation, or an assemblage of both (Figures 4B and 5). The presence of fine-grained carbonate
239 in the siliciclastic matrix, with or without magnetite, indicates slumping before lithification of all
240 the carbonate and many of the siliciclastics. There are also contorted layers where cm-scale
241 calcite laminae behaved brittlely and mm-scale magnetite laminae behaved ductilely. These
242 represent slumped carbonate - magnetite lithofacies, where the calcite layers were, at least,
243 partially lithified and the iron oxide layers were not. The contorted, convolute laminated and
244 brecciated zones in places are overlain by cm-scale layers of calcite and magnetite. This
245 lithofacies is associated with the carbonate - magnetite lithofacies, though with a larger content

of magnetite. All of the above show no evidence of bottom current activity, placing deposition below storm wave base.

Tectonic brecciation is unlikely as none of the other lithofacies show any indication of tectonic brecciation, the facies overlying and underlying the slumped units are parallel laminated, and the broken carbonate layers/clasts are randomly oriented. Hence, it is assumed that soft-sediment deformation due to slope instability in the outer carbonate-dominated area of the platform led to the development of the slumped carbonate facies, where the displaced carbonate mixed with other non-lithified sediments as it moved down-slope and eventually interbedded with the sediments of those areas.

Oxide-Facies Iron Formation

The oxide-facies iron formation (OFIF) is characterized by magnetite interlaminated with chert. Hematite is absent in the Red Lake stratigraphy. Fine-grained black magnetite bands of 2-5 cm thickness are interlayered with light colored chert bands of similar thickness (Figure 6A). Granular iron formation and current formed structures are absent. Chert bands are typically white to grey, with color variation dependent on their incorporation of siliciclastic and carbonaceous materials. Magnetite layering is straight to slightly wavy, parallel, laterally continuous, and commonly has sharp contacts with the chert bands but in some places, contacts are gradual (Figures 6A and 6C). OFIF is exposed and laterally continuous up to tens of meters near the shoreline of the east side of Bridget Lake. In this outcrop, OFIF occurs together with chert, sulfidic slate, and siltstone while approximately 1.5 km east from this outcrop, it appears with massive chert and sulfidic slate (Outcrop - 3 in Figure 1 and Figure 6B). In core samples, the proportion of magnetite and chert bands varies. This yellowish lining at the contact of chert and magnetite band is grunerite, which is a common iron silicate mineral found in regionally

metamorphosed terrains (Figure 6C). Drill holes located in the eastern and central part of the Red Lake area have OFIF that alternate with chert, sulfidic iron formation, siltstone, and are overlain and underlain by dolomitic carbonate. Drill hole core containing OFIF from the Pancake Bay area is mostly associated with dolomitic carbonates, and to a lesser extent with chert.

Massive Chert

Successions of white to grey, massive chert vary from a few meters in thickness to 10 meters. In drill holes it appears fractured with no visible laminations. The massive chert layers are associated with magnetite bands of variable thickness and separated by siltstone, black slate, and/or sandstone. At one location massive chert beds of 10 to 15 cm thickness, but rarely up to 30 cm in thickness, are present in outcrop along with carbonaceous, sulfidic slate, and OFIF (Outcrop - 3 in Figure 1 and Figure 6B). The thick, parallel and straight chert beds are, in places, separated by thin magnetite bands with sharp contacts.

Sulfidic Slate

The sulfidic, carbonaceous slate is commonly associated with carbonaceous slate and contains pyrite and/or pyrrhotite. In drill-holes these intervals range from 5 to 25 m thick and are associated with units of oxide-facies iron formation in addition to non-sulfidic slate overlain and underlain by dolomitic carbonate-chert assemblages. This type of deposit is easily identifiable in outcrops because of the appearance of gossan, and in places by pyrite nodules (Outcrop - 3 in Figure 1 and Figures 7A and 7B). It is better preserved in core samples where iron sulfides are interlayered with black slate or disseminated as small particles or larger, recrystallized cubes. In slabbed core samples, pyrite is dull golden to brass yellow blobs and/or laminae of variable thickness, ranging from a few millimeters to centimeters, which alternates with black slate

291 (Figures 7C and 7D) while pyrrhotite usually occurs as dark bronze-colored patches to well-
292 layered laminae.

293 SEM elemental mapping highlights large euhedral pyrite recrystallized over anhedral
294 pyrrhotite, with the recrystallized pyrite exhibiting typical polygranular textures (Figure 7E).
295 This type of co-occurrence indicates the iron sulfides have undergone replacement reactions;
296 hence, original phases are difficult to ascertain. Very small amounts of chalcopyrite and
297 sphalerite are also present and are reflected in whole rock analyses of the sulfides (Zn in pyrite =
298 range 41 to 1720 ppm, mean= 605 ppm; Cu in pyrite = range 51 to 3100 ppm, mean= 600 ppm;
299 Zn in pyrrhotite = range 55 to 150, mean= 92 ppm; Cu in pyrrhotite = range 47 to 570, mean=
300 225 ppm).

301 **Black Slate**

302 Black slates are organic carbon-rich (TOC up to 5 % with $\delta^{13}C$ -30 to -17 ‰) mudstones,
303 which are rare in outcrop because of weathering but are well-preserved in drill core. They have
304 no visible sedimentary structures. The thickness of black slate units in the drill holes varies from
305 a few meters to 40 meters. These successions are associated with sulfidic slate and siltstone, and
306 in places underlain by dolomitic carbonate-chert, and overlain by calcitic carbonate-sandstone-
307 dolomitic carbonate packages in the drill holes. The fine-grained siliciclastics are mainly
308 composed of muscovite, feldspar, and quartz. Sulfide content in black slates varies, and pyrite
309 often appears as thin laminae, disseminated small cubes, and irregular aggregates. These form a
310 continuum with the sulfidic slates.

311 **4.2. Geochemistry Results**

312 The concentrations of major elements in the deep water facies of the Red Lake platform
313 are typical for their respective lithologies. Red Lake black slates show mean compositions

314 similar to the continental crust (15.7 wt.% Al_2O_3; 0.3 wt.% TiO_2; 2.7 wt.% K_2O; 1.6 wt.% CaO;
315 1.3 wt.% MgO; 5.8 wt.% total Fe_2O_3; 0.2 wt.% MnO). Isolated pyrite and pyrrhotite minerals of
316 the sulfidic slates show concentrations of Fe ranging from 37.0 to 69.2 wt.% (mean 54.6 wt.%).
317 The iron formation samples have total Fe_2O_3 values ranging from 25.7 to 77.2 wt.% (mean 51.8
318 wt.%) and MnO values ranging from 0.1 to 6.3 wt.% (mean 1.3 wt.%); in contrast, the chert
319 samples have total Fe_2O_3 ranging from 0.2 to 1.1 wt.% (mean 0.5 wt.%) and MnO ranging from
320 0.004 to 0.2 wt.% (mean 0.05 wt.%). The carbonate samples have CaO ranging from 7.9 to 43.2
321 wt.% (mean 19.3 wt.%), MgO ranging from 0.2 to 8.8 wt.% (mean 2.7 wt.%); total Fe_2O_3
322 ranging from 0.3 to 2.6 wt.% (mean 1.3 wt.%), and MnO ranging from 0.2 to 0.7 wt.% (mean 0.4
323 wt.%).

324 Major elements that are predominately derived from clastic sources, such as Al_2O_3 and
325 TiO_2, are proxies for siliciclastic contamination, and they are generally low for the Red Lake
326 chemical sediments, ranging from 0.09 wt.% to 0.46 wt.% and 0.001 wt.% to 0.005 wt.%
327 respectively for the analyzed carbonates. The iron formation shows variable degrees of detrital
328 contamination, with Al_2O_3 contents <0.5 wt.% indicating highly pure chemical sediment with an
329 insignificant presence of siliciclastic material, while high Al_2O_3 (>1 wt.%) indicating siliciclastic
330 contaminated samples. Chert samples have very low Al_2O_3 and TiO_2 contents, ranging from
331 0.039 wt.% to 0.15 wt.% and 0.001 wt.% to 0.006 wt.% respectively.

332 Cross-plots of Al_2O_3 and TiO_2 vs. Cr, Mo, V, and U (Figure 8) show overall positive
333 linear correlations. However, some samples deviate from the linear correlation due to excess of
334 the redox-sensitive element, i.e., excess Cr in the majority of carbonates, excess Mo in most
335 sulfides, chert and carbonates, excess V in magnetite, and excess U in carbonates. To assess the
336 relative enrichment of redox-sensitive elements in chemical sedimentary rocks, Enrichment

337 factors (EF) were calculated using the formula: $(TM/TiO_2)_{EF} = [(TM/ TiO_2)_{sample} / (TM/ TiO_2)_{average\ shale}]$, where TiO_2-normalized trace metal (TM) concentration is compared to the
339 average shale value (Wedepohl, 1991, 1971). When EF is >1, it indicates trace metal enrichment
340 relative to what is expected from the siliciclastic components of the sample (Wedepohl, 1991,
341 1971). From the enrichment factor plot of Cr, Mo, V, and U (Figure 9), it is obvious that most of
342 the carbonate samples have higher concentrations of Cr than expected to derive from their
343 siliciclastic components. Mo enrichments are notable in almost all samples. Most of the
344 magnetite and pyrite-pyrrhotite samples are enriched in V, whereas all carbonate samples have V
345 concentrations that are below detection. Carbonate samples are enriched in U compared with
346 most of the magnetite and chert samples, which show some enrichment, and the sulfide samples,
347 which are similar to the black slate. This may be due to uranium's ability to fit into the carbonate
348 lattice.

349 For Archean carbonates and iron formations, the Y/Ho mass ratio is generally > 44 g/g
350 and > 40 g/g, respectively (Kamber and Webb, 2001; Planavsky et al., 2010). The Y/Ho ratios of
351 Red Lake carbonates average 51 while they average 42 for iron formation and chert (Figure 10).
352 All of these Y/Ho ratios are noticeably higher than the PAAS ratio of 27 g/g. In contrast, the
353 black slate and the sulfidic slate samples have average Y/Ho ratios of ~27 and ~25, respectively,
354 similar to the chondritic Y/Ho ratio.

355 PAAS-normalized Eu anomalies for Archean iron formations normally range from 1.0 to
356 4.29 (average 2.1) (Planavsky et al., 2010). Among the chemical sedimentary rocks of Red Lake,
357 the oxide-facies iron formation samples have Eu anomalies between 1.4 and 3.24, with an
358 average of 2.3, which is similar to other typical Archean iron deposits, e.g. those of the
359 Geraldton and Terrace Bay areas, north of Lake Superior, Canada; the Kuruman iron formation,

South Africa; and BIF of the Warrawoona Group, Pilbara Craton, Australia (Barrett et al., 1988; Bau and Dulski, 1995; Bolhar et al., 2005; Planavsky et al., 2010). Similar to the iron formations, the deeper water carbonate rocks at Red Lake exhibit positive Eu anomalies ranging from 1.1 to 3.5, with an average of 2.1, while chert ranges from 1.5 to 2.4 with an average of 2.3 (Figure 11). The black slates, pyrites, and pyrrhotites have smaller positive Eu anomalies, averaging 1.7, 1.3, and 1.5, respectively (Figure 11). All samples also have positive Gd anomalies, generally ranging from 1.1 to 1.5 (Figure 11). Most carbonate and iron formation samples from Red Lake are also LREE depleted to varying degrees (Figures 12 and 13). Conversely, most chert, iron sulfides, and black slate either have flat REE patterns or are LREE enriched.

A cross-plot of Pr/Pr* vs. Ce/Ce* as per Bau and Dulski (1996a) shows that roughly half of the oxide iron formation and carbonate samples and the majority of chert samples plot in the positive La and positive Ce anomaly fields (Figure 14). Almost all the sulfide and black slate samples plot in the zone reflecting an absence of La or Ce anomalies. One carbonate sample that was deposited on the slope close to the shallow water carbonates has a negative Ce anomaly.

5. Discussion

5.1. Geochemical signatures of Mesoarchean seawater chemistry

Enrichments in redox-sensitive trace elements, i.e., chromium (Cr), molybdenum (Mo), vanadium (V), and uranium (U), in ancient marine deposits are powerful proxies of oxygenation of the atmosphere and oceans prior to and during the Great Oxidation Event (GOE) (Anbar, 2007; Crowe et al., 2013; Frei et al., 2009; Planavsky et al., 2014; Rosing and Frei, 2004; Wille et al., 2013). These elements are delivered to seawater largely via oxidative continental weathering, during which they are more mobile in higher valence states, depending on the

382 presence of oxygen (Calvert and Pedersen, 1993; Morford et al., 2001; Russell and Morford,
383 2001; Voegelin et al., 2010; Wille et al., 2013). The gradual rise of atmospheric oxygen before
384 the GOE is interpreted as key to the initiation of widespread oxidative chemical weathering of
385 crustal rocks and transport of these elements to the ocean via river runoff (e.g., Frei et al., 2009;
386 Konhauser et al., 2011; Robbins et al., 2016; Sahoo et al., 2012). Redox-sensitive trace metal
387 enrichments were examined in this context to investigate atmosphere-ocean redox conditions
388 during the deposition of the Red Lake carbonate platform. The concentrations of Cr, Mo, V, and
389 U plotted against Al_2O_3 and TiO_2, as well as the enrichment factors plot of Cr, Mo, V, and U for
390 various lithofacies clearly show that the chemical sedimentary rocks have variable degrees of
391 enrichment of these elements relative to their siliciclastic associates. The source of redox-
392 sensitive elements in the basin was either high-temperature hydrothermal fluid or fluvial
393 discharge. The presence of oxygen is not necessary for hydrothermal input, but for the latter
394 possibility, oxygen would be indicated in the weathering environment to mobilize these
395 elements. The enrichment of the redox-sensitive elements in the samples of chemical
396 sedimentary rocks indicates aqueous scavenging from seawater into the chemical sediments
397 through either high-temperature hydrothermal fluids or fluvial discharges that bore witness to
398 mild oxidative weathering.

399 The REE systematics of chemical sediments in particular are largely controlled by local
400 seawater chemistry (Barrett et al., 1988; Bau and Dulski, 1996a; Bau and Möller, 1993; Bekker
401 et al., 2010; Bolhar et al., 2004; Danielson et al., 1992; Derry and Jacobsen, 1990; Kamber and
402 Webb, 2001; Planavsky et al., 2010; Van Kranendonk et al., 2003). REE in seawater can come
403 from a variety of sources, including river runoff, hydrothermal input, and aeolian transport and
404 settling of fine-grained sediment through the water column (Elderfield, 1988). The degree of

405 detrital contamination of chemical sedimentary rock is a critical parameter for evaluating REE
406 patterns as siliciclastic materials rapidly dilute and mask the REE signature of low-REE-
407 abundance chemical precipitates (Allwood et al., 2010; Bau and Möller, 1993; Planavsky et al.,
408 2010). Furthermore, REEs can substitute in carbonate and are adsorbed by iron hydroxides,
409 resulting in these chemical participates having greater levels of REEs than cherts and sulfides,
410 which will neither adsorb nor readily permit substitution of REEs. Thus, the amount of
411 siliciclastics that will interfere with the REE patterns of chert and sulfides is far less than that
412 needed to have a significant impact on magnetite and calcite or dolomite. Pure tetrahedral silica
413 should not contain REE, and it is likely that other phases are carrying the majority of REE in
414 these samples. Likewise, the phase in the sulfides that is associated with a significant amount of
415 REE may not be the sulfide minerals themselves.

416 Siliciclastic mixing can obscure primary seawater signatures, such as La, Ce, Eu, and Gd
417 anomalies, and flatten REE patterns (Peter, 2003; Webb and Kamber, 2000). The common
418 characteristics of modern seawater when shale-normalized are: positive La anomalies, negative
419 Ce anomalies, slightly positive Gd anomalies, slight negative Eu anomalies, depletion of LREEs
420 relative to HREEs, and super-chondritic Y/Ho ratios greater than ~44 g/g (Bolhar et al., 2005;
421 Bolhar and Van Kranendonk, 2007; Planavsky et al., 2010; Shields and Stille, 2001). The high
422 Y/Ho ratio is a useful indicator for monitoring siliciclastic contamination affecting REE patterns.
423 Siliciclastic influence can be determined by plotting the Y/Ho ratio against immobile elements
424 common in siliciclastic rock such as Al_2O_3 or TiO_2 (Bolhar et al., 2004; Kamber and Webb,
425 2001). The Y/Ho mass ratio of crustal rocks ranges from 26 to 28 (Kamber and Webb, 2001)
426 while for modern seawater it varies between 44 and 120 but can be depressed back to ~27 by the
427 addition of siliciclastics and/or volcanic ash to seawater precipitates (Bolhar et al., 2004; Nozaki

et al., 1997; Webb and Kamber, 2000). Insignificant siliciclastic contamination is suggested by the super chondritic Y/Ho ratios of most carbonate and iron oxide-bearing chemical sedimentary rocks (Figure 10A). Some iron sulfide samples have Y/Ho ratios similar to chondritic ratios (i.e., 27) of crustal rocks, indicating that these samples have their REE patterns controlled by siliciclastic contamination (Bolhar et al., 2004; Kamber and Webb, 2001). Y/Ho ratio vs. slope of the REE pattern (Figure 10B) reveals carbonate and oxide iron formation samples generally with higher Y/Ho ratios and lower Pr/Yb ratios, the latter reflecting HREE enrichment that is also typical of seawater.

Eu anomalies occur when Eu(III) is reduced to Eu(II) and scavenged from mafic igneous rocks during hydrothermal circulation at temperatures above 250° C (Danielson et al., 1992; Peter, 2003). Thus, a positive Eu anomaly is indicative of high-temperature hydrothermal inputs into the ocean where high-temperature fluid circulation leached Eu(II) from oceanic crust, replacing Ca^{+2} in plagioclase feldspar, similar to modern marine exhalative precipitates (Danielson et al., 1992; Derry and Jacobsen, 1990; Fowler and Doig, 1983; Klinkhammer et al., 1983, 1994). The omnipresence of similar Eu anomalies (Figures 11 and 12) and slopes of the REE patterns in the shallow water stromatolitic carbonates (McIntyre and Fralick, 2017) and deeper water fine-grained carbonates and oxide facies iron formation lacking evidence of current activity, and therefore very likely deposited below storm wave base, indicates that the Mesoarchean ocean had a positive Eu anomaly produced by high-temperature hydrothermal inputs, and these rocks inherited the REE composition of the Mesoarchean seawater (Figure 15). The positive Gd anomalies present in the chemical and siliciclastic sedimentary rocks may be due to Gd scavenging by organic matter, as extrapolated from the observation of Gd anomalies in modern wastewater (Bau et al., 1996; Bau and Dulski, 1996b).

Modern and Archean seawater are LREE-depleted compared to PAAS values (Barrett et al., 1988; Bolhar et al., 2004; Planavsky et al., 2010; Zhang and Nozaki, 1996). HREE enrichment is present in the carbonate and iron formation samples, typical of seawater (Allwood et al., 2010; Bolhar et al., 2005), while LREE enrichment is present in the chert, pyrite, and pyrrhotite samples (Figure 12; Figure 13), typical of felsic detritus. The Eu anomaly, Gd anomaly, and the REE patterns in general present in chert and iron sulfides, i.e., the pyrite and pyrrhotite samples (Figure 15), are most likely the result of micro-inclusions of other materials as REE do not fit into the lattice framework of pure chert, and fluid inclusions and substitutions in crystal defects can produce deceptive REE patterns in iron sulfides (Zhao and Jiang, 2007). Thus, their REE patterns do not reflect seawater, but rather are likely controlled by the incorporation of intermediate to felsic siliciclastic material, which, even though very scarce in some samples, was able to overwhelm any REEs that were derived from seawater. In addition, the comparable Y/Ho ratios and flat REE patterns of the black slate and sulfide samples (Figure 15) indicate that the main phase carrying REE in the sulfides are siliciclastics comparable in composition to the original clays in the black slates. This is undoubtedly due to the fact that iron sulfides do not scavenge appreciable REE from seawater, and REE substitution is highly unfavorable in their lattice.

Shale-normalized Ce anomalies record ancient redox conditions of the oceans (Allwood et al., 2010; Bolhar et al., 2005; Planavsky et al., 2010; Shields and Stille, 2001). When Ce(III) is oxidized to Ce(IV), it becomes is highly particle reactive and insoluble, and therefore precipitates or is preferentially scavenged onto Fe-Mn oxyhydroxide surfaces (Bau and Dulski, 1996a; Bolhar et al., 2004; Planavsky et al., 2010; Sholkovitz et al., 1994; Tostevin et al., 2016a). Later precipitates from the fluid inherit the resulting anomaly. A negative Ce anomaly is

474 a common feature of modern oxic seawater (Elderfield and Greaves, 1982; Goldberg et al.,
475 1963). The detection of Ce anomalies in marine precipitates can be complicated because of the
476 anomalous abundance of La and a false negative Ce anomaly may arise if using the equation
477 $Ce/Ce^*=Ce/(0.5La_{PAAS}+0.5Pr_{PAAS})$. Therefore, Ce/Ce* vs. Pr/Pr* anomalies were plotted to
478 distinguish true negative Ce anomalies as recommended by Bau and Dulski (1996a), where
479 $Pr/Pr^*=Pr/(0.5Ce_{PAAS}+0.5Nd_{PAAS})$ and La_{PAAS}, Ce_{PAAS}, Pr_{PAAS}, and Nd_{PAAS} denote the PAAS
480 normalized values. In this approach, values of Ce/Ce* <0.95 and Pr/Pr* >1.05 is indicative of a
481 true negative Ce anomaly (Bau and Dulski, 1996a), which is the case for modern seawater.
482 However, values of Ce/Ce*< 0.95 without corresponding positive Pr/Pr* anomalies indicates a
483 false negative Ce anomaly due entirely to the presence of a positive La anomaly. The presence of
484 a positive La anomaly, i.e., enrichment of La relative to Ce, is an indication of an
485 uncontaminated marine REE signature in shale-normalized REE patterns (Bau and Dulski,
486 1996a; Kamber and Webb, 2001).

487 Ce anomalies can be further investigated using Mn as the two elements have similar
488 reduction potentials and Ce^{3+} can be oxidized to Ce^{4+} on the surface of Mn oxides (Takahashi et
489 al., 2002; Tostevin et al., 2016a, 2016b). This leads to an association between positive Ce
490 anomalies and concentrations of Mn in precipitates if sufficient O_2 is present in the water mass,
491 and provides a useful proxy for O_2 (Gauthier-Lafaye and Weber, 2003; Ossa Ossa et al., 2016;
492 Roy, 2006; Tostevin et al., 2016; Tsikos et al., 2010; Warke et al., 2020). Manganese is enriched
493 in most iron formation samples from Red Lake, with an average of 1.3 wt.%. Higher values are
494 concentrated in oxide iron formation directly underlying the carbonate platform and generally
495 increase towards the platform. This contrasts with Mn concentrations predominantly less than 1

496 in samples of oxide iron formation deposited above the carbonate platform after it was
497 transgressed, and carbonate deposition came to an end in the area.

498 The positive Ce anomalies in the oxide facies iron formations and in seven carbonate
499 samples (Figure 14) suggest the presence of some oxygen in the Mesoarchean offshore during
500 the deposition of iron hydroxides and calcite, where Ce was mildly oxidized and preferentially
501 precipitated from seawater compared to the other rare earth elements. This is also manifest by the
502 elevated amounts of Mn in the oxide facies iron formation near the carbonate platform. The Mn^{2+}
503 in the offshore water near the carbonate portion of the platform was oxidized by O_2 and
504 precipitated with the Fe^{3+} hydroxides that were, likewise, oxidized. As Ce oxidizes under similar
505 partial pressure of O_2 to Mn, and Ce^{3+} can be oxidized to Ce^{4+} on the surface of Mn oxides
506 (Takahashi et al., 2002; Tostevin et al., 2016a, 2016b) it is probable that the positive Ce
507 anomalies developed due to the presence of O_2.

508 In summary, the carbonates and oxide facies iron formations of Red Lake have high
509 positive Eu anomalies, suprachondritic Y/Ho ratios, and low Pr/Yb ratios. These results indicate
510 that the shelf environment was heavily influenced by Archean seawater with a hydrothermal
511 component. The oxidation and removal of Ce and Mn from seawater leading to the enrichment of
512 these elements in chemical sediments near the carbonate portion of the platform points to the
513 presence of O_2, at least temporarily, in the depositional environment.

514 **5.2. Offshore Depositional Environments of the Red Lake carbonate platform**

515 The alternating precipitation of calcitic carbonate and magnetite layers in carbonate -
516 magnetite strata unveil interesting characteristics of the depositional environment. These were
517 observed in the field (Fig 1, outcrop locations 1 and 4) but were not positively identified in the

518 industry drill cores. Field observations reveal that stratigraphically, the carbonate - magnetite
519 lithofacies and underlying slumped and mass-flows of carbonate in a matrix of magnetite and/or
520 slate, with no evidence of wave activity, are overlain by stromatolitic carbonate with current
521 eroded areas (McIntyre and Fralick, 2017), and very likely deposited in the photic zone (Fig. 2
522 inset). Such stratigraphic positioning indicates the carbonate interlayered with magnetite and
523 mass-flows are transitional facies between the shallow water carbonate facies and deeper-water
524 oxide facies iron formation. The massive nature of the calcite here, lacking any obvious
525 microbialite features or sedimentary textures that may indicate clastic redeposition of carbonate
526 eroded from the shallow-water stromatolitic carbonates, as well as the presence of crystal fans
527 elsewhere in the platform indicative of aragonite needle growth at times on the seafloor
528 (McIntyre and Fralick, 2017), indicates that precipitation of Ca-carbonate may have occurred in
529 the water column, driven by seawater supersaturated with calcite or aragonite. Iron hydroxide
530 precipitation could have been caused by a number of processes. One possibility is that periods of
531 onshore directed current flow may have reduced the extent of shallow water carbonate saturation
532 and allowed the slower accumulation of iron hydroxides to dominate, perhaps accompanied by
533 landward movement of an oxycline. Conversely, storm generated geostrophic flows could have
534 delivered trace amounts of oxygen to the transitional area, where carbonate had been
535 precipitating, causing a brief change to iron hydroxide precipitation (Pufahl and Fralick, 2004).
536 While both mechanisms are somewhat speculative, the former is supported by hiatuses between
537 carbonate and magnetite precipitation that are evident from the deposition of very thin laminae of
538 what was originally mud between the carbonate and magnetite layers (Figure 16). Also, the
539 magnetite layers have more mud in them than the carbonate layers. If this depositional system
540 was similar to offshore depositional systems today, mud was the background sediment, slowly

and continuously being deposited by rainout. Thus, larger amounts of mud mixed with chemical sediment denote slower deposition rates of the chemical sediment (Pufahl and Fralick, 2004). A scenario can be envisioned whereby offshore-directed storm-derived currents delivering oxygen caused rapid precipitation of iron hydroxides (Pufahl and Fralick, 2004), whereas upwelling ocean currents will both delivered colder water under-saturated in bicarbonate, shutting down calcite precipitation, and forced the oxycline shoreward into the area previously precipitating carbonate, favoring iron hydroxide precipitation. In this manner, periods of upwelling of deeper waters may have driven the change to iron hydroxide precipitation, although other scenarios are also possible, and additional future study of these relatively unique lithofacies juxtapositions is warranted.

Stratigraphically, the carbonate mass-flow and slump facies is seated underneath and offshore from the laminated carbonate facies that was deposited in peritidal settings (McIntyre and Fralick, 2017). On the Red Lake carbonate platform, two types of carbonate mass-flows occur – (i) magnetite-hosted carbonate mass-flows and (ii) slate-hosted carbonate mass-flows. The carbonates of deep subtidal to upper slope depositional settings were probably slumped due to slope instability and became disorganized mass-flows below the photic zone where no carbonate was being deposited. As the mass-flow of carbonate moved downslope through areas of mud and/or oxide facies iron formation, it incorporated some of this material, which, upon coming to rest, mixed with particulate carbonate to form the matrix surrounding the carbonate clasts. This indicates that some of the offshore carbonates were likely undergoing early cementation at the seafloor, as occurs widely in modern carbonate platforms.

The position of oxide iron formation, black slate, and pyritiferous black slate directly underlying the stromatolitic carbonate (Figure 2) indicate that the siliciclastic and ferruginous

564 deposits were directly offshore from the carbonates. The mass-flows denote that there was a
565 slope separating the carbonate inner shelf from the iron formation and fine-grained siliciclastics.
566 Due to the sporadic and very limited occurrence of mass-flows and carbonate-magnetite
567 lithofacies, the extension of the slope environment is uncertain.

568 The lithofacies zones from on-shore to offshore are therefore: 1) A broad zone of
569 peritidal dolomitic carbonate with coliform crusts, thin layers of crystal fans, grainstones, and
570 abundant *Stratifera* and *Colleniella* stromatolites (McIntyre and Fralick, 2017); 2) A subtidal
571 area that is dominantly calcic carbonate with *Stratifera* and ~ 1m Atikokania crystal fan mounds
572 in shallower regions and larger crystal fan mounds further offshore (McIntyre and Fralick, 2017);
573 3) A sporadically developed minor slope composed of carbonaceous mud and iron formation
574 with carbonate-magnetite laminae at its crest and slump deposits mixing these lithologies
575 together; 4) At the base of slope and in other areas adjacent to carbonate where the slope was not
576 present, the bottom varied vertically, and possibly laterally, between the accumulation of
577 carbonaceous mud, sulfide laminae in carbonaceous mud, oxide iron formation, chert, and
578 siltstone-sandstone. The vertical organization of these lithofacies is best observed in cored drill
579 hole EBL 10-27 (Figure 2). In this drill hole the lithologies underlying the carbonate strata on the
580 shelf begin with a 16 m thick chert-sandstone-siltstone assemblage that is overlain by 12 m of
581 carbonaceous slate with thin oxide iron formation both below and above it. This is followed by
582 10 m of sulfide-rich carbonaceous slate, which is overlain by 18 m of oxide iron formation with
583 one 2 m thick sulfidic, carbonaceous slate in it. There are then 20 m of chert with siltstone layers
584 and 25 m of siltstone and sandstone with chert layers. The succession is capped by 33 m of chert
585 with increasing zones of oxide iron formation upwards. The shallow water carbonate portion of
586 the shelf overlies this (Figure 2). Zones of non-carbonate sediment such as this highlight the

587 variability of deposit types that were capable of accumulating on and around the margins of the
588 carbonate platform.

589 The condensed successions of carbonaceous slate with their high organic carbon contents
590 suggests deposition below wave base from background clay and biologic rainout onto the
591 bottom. The Fe-sulfide layers have very low amounts of clay and carbon, indicating they
592 represent relatively rapid depositional events compared to the organic-rich mud. The large
593 amounts of Zn and Cu in some of the iron sulfide layers signify an origin from discrete
594 hydrothermal plume events (cf. Fralick et al., 1989; Goodwin, 1973). However, others have low
595 amounts of Zn and Cu, implying a hydrogenous origin. The sulfur has three possible sources: 1)
596 reduction of seawater sulfate, 2) thiolated species from hydrothermal fluid, 3) decay of biomass
597 releasing organic sulfur, and the combination of sources may have varied depending on the rate
598 of precipitation. The co-occurrence of irregularly laminated to nodular pyrite in association with
599 carbonaceous slate reflects the probable presence of microbial communities in the sediment that
600 were influencing porewater chemistry (Gregory et al., 2019; Wright and Altermann, 2000).
601 However, infrequent discharges of iron-rich solutions from a relatively low-temperature diffuse
602 hydrothermal venting system into an anoxic bottom water layer may have driven the mm- to cm-
603 scale pyrite and pyrrhotite laminations and banding within carbonaceous mud layers (Fralick et
604 al., 1989; Hofmann, 2011).

605 Oxide facies iron formation is interlayered on the meter-scale with sulfidic, carbonaceous
606 slates. The obvious difference is the oxidation state of the iron. Iron sulfides are only
607 interlaminated with carbonaceous fine-grained sediment, while the Red Lake magnetite layers
608 are never interlayered with carbonaceous sediment. In these successions, chert is uniquely
609 interlaminated with magnetite. The extreme reducing conditions caused by the elimination of O_2

610 during the degradation of organic matter in the fine-grained sediment would have precluded the
611 formation of iron oxides and led to the association of iron sulfides and organic-rich slates. The
612 presence of diagenetically produced euxinic areas caused by concentrations of organic matter in
613 sediment has negative implications for the use of sulfidic, carbonaceous shales/slates to infer
614 euxinic conditions in the global ocean (Meyer and Kump, 2008; Poulton et al., 2010). The
615 possibility of diagenetic control of oxidation state, either in the sediment or a stagnant bottom
616 water layer, should be investigated prior to assuming the presence of iron sulfides, not oxides,
617 infers an euxinic ocean.

618 Chert, siltstone-sandstone, and oxide iron formation dominate closer to the base of the
619 stromatolitic carbonate succession. The alternation between these lithofacies requires that their
620 sedimentation was turning on and off, and when they were being deposited, their accumulation
621 rates were much higher than that of the organic-rich mud. This is obvious for the sandstone-
622 siltstone layers, which would represent discrete depositional events of sediment derived from
623 erosion of the landmass washed onto the shallow shelf during storm events and extending into
624 the further offshore areas. The low siliciclastic content of the magnetite and some of the chert
625 layers suggests their relatively rapid accumulation. To explain the deposition of oxide facies iron
626 formation, it is hypothesized that an offshore, ferrous (Fe^{+2}) iron-rich water mass reacted with an
627 oxygen-producing or slightly oxygenated water mass in the vicinity of a redox boundary in the
628 water column separating the stromatolite-rich shallow shelf from the further offshore lithofacies,
629 similar to what has been inferred for the Steep Rock Lake Group (e.g., Fralick and Riding, 2015;
630 Riding et al., 2014). This resulted in the accumulation of ferric oxyhydroxides or hydroxides on
631 the bottom, which are eventually transformed to magnetite during diagenesis.

632 The deposition of silica was probably non-biogenic as the Archean ocean was devoid of
633 silica-secreting organisms (Cloud, 1973; Delvigne, 2012; Holland, 1974; Maliva et al., 2005).
634 The silicon concentration in Archean hydrothermal fluids can theoretically be 4 to 7 times
635 greater than the concentration in modern hydrothermal fluids (i.e., 1680-3000 ppm in Archean
636 vs. 450-650 ppm in modern time) (Delvigne, 2012; Mortlock et al., 1993; Shibuya et al., 2010;
637 Van den Boorn, 2008; Wang et al., 2011). Therefore, it is assumed that the source of silica in the
638 Archean ocean was largely hydrothermal, and silicic acid (H_4SiO_4)-saturated marine conditions
639 drove the deposition of silica (Barrett et al., 1988; Cloud, 1973; Gross and Zajac, 1983; Holland,
640 1973; Maliva et al., 2005; Siever, 1992, 1957). Rapid precipitation from low-temperature silica-
641 rich hydrothermal fluids probably triggered the deposition of massive chert. The alternative, that
642 the presence of silica-saturated seawater in a low energy environment caused the slow
643 evaporative precipitation of regular, flat, laterally continuous chert laminae, is problematic as
644 these settings were dominated by mud. Therefore, chert deposition had to turn on and off, or the
645 background sediment would be mud-rich chert, not mud without chert. However, the
646 mechanism(s) controlling alternation of precipitation of iron oxide and chert precipitation itself
647 are not understood.

648 **5.3 Significance of the Red Lake carbonate platform and its offshore facies**

649 The Red Lake carbonate platform is globally unique in terms of known Paleoarchean to
650 Mesoarchean sedimentary deposits for several reasons. First, substantial occurrences of
651 sedimentary carbonate are rare to absent in the earliest sedimentary records. Riding et al. (2014)
652 compiled the known thicknesses of Archean sedimentary carbonates, and the Red Lake
653 carbonate platform stands out as the first sedimentary carbonate occurrence to exceed 100 m in
654 thickness; as seen in this combined drill core and field study, it is now clear that the Red Lake

carbonate platform preserves an estimated total of 250 m of dolomite and calcite in terms of true stratigraphic thickness. The most comparable thick carbonate deposits in the 3.0 to 2.8 Ga window are the 2.96 Ga Chobeni carbonate of the Pongola Supergroup and the 2.80 Ga Mosher carbonate of the Steep Rock Group. In the case of the Chobeni carbonate, it's approximately 50 m of sedimentary carbonate is composed largely of reworked clastic carbonate, carbonate sand microbialites, and to a lesser degree, chemically sedimented microbialites (Siahi et al., 2018, 2016); in the case of the Mosher carbonate, over 400 m of carbonate microbialite and crystal fans are preserved (Riding et al., 2014), with little evidence of sedimentary reworking or clastic carbonate redeposition. The Red Lake carbonate platform, intermediate in age between these two deposits, thus captures a "ramping up" of Earth's carbonate factory, whereby thicker and thicker occurrences of carbonate are expressed in the sedimentary rock record over the 3.0 to 2.5 Ga window, ultimately cumulating in the deposition of the 2.59 - 2.52 Ga Campbellrand-Malmani carbonate platform that achieves over 2 km of thickness (Beukes, 1987; Knoll and Beukes, 2009; Sumner and Grotzinger, 1996).

The Red Lake carbonate platform is also relatively unique in terms of Mesoarchean sedimentary deposits with respect to the offshore sedimentary facies that punctuate the carbonate platform throughout its entire thickness. Indeed, several drowning events, indicated by the occurrence of black slates and iron formation, can be observed through the sequences suggesting fluctuating sea levels and consequent changes in seawater chemistry in the Red Lake depositional basin. Carbonate growth resumes after flooding, keeping up with subsidence over hundreds of meters. By comparison, the Chobeni carbonate shows no such deep water facies and has been interpreted as a tide-dominated shallow water clastic-carbonate system (Siahi et al., 2016), whereas deeper water shales and iron formation are restricted to the overlying Mozaan

678 Group (Smith et al., 2020). Steep Rock carbonates have conformable contact with deeper water
679 iron formation facies but do not show comparable periodic sea level variations (Fralick et al.,
680 2008). The Campbellrand-Malmani carbonate platform also does not contain abundant shale or
681 iron formation in its stratigraphy. Red Lake thus appears unique in this respect in that repeated
682 transitions between offshore and onshore facies are evident, as well as intermediate facies (e.g.,
683 carbonate slump in iron formation and in carbonaceous shale).

684 Finally, the 2.93 Ga age of the Red Lake carbonate platform places it at a critical junction
685 in the redox evolution of Earth's oceans. Some of the earliest evidence for oxygenic
686 photosynthesis, thought to occur in ephemeral and/or spatially restricted oxygen oases (Lalonde
687 and Konhauser, 2015; Olson et al., 2013), begins to express itself in the rock record ca. 3.0 to 2.8
688 Ga in both shallow water and deep water chemical sediments. For example, in the Pongola
689 supergroup, paired Fe-S isotope systematics of the Chobeni carbonate have been used to argue
690 for local oxygenic photosynthesis (Eickmann et al., 2018), which is further supported by Ce
691 abundance anomalies (Siahi et al., 2018; Thoby et al., 2019) as well as Mo stable isotope
692 evidence (Thoby et al., 2019). In deep water water facies of the overlying Mozaan group, U
693 enrichments and Cr isotope data (Crowe et al., 2013), as well as Mo stable isotope compositions
694 that scale with Fe/Mn (Albut et al., 2019, 2018; Planavsky et al., 2014) have all been used to
695 indicate localized oxygen production ca. 2.96 Ga. Red Lake carbonate platform, preserving both
696 shallow and deep and uniquely preserving sulfidized slates that in themselves may indicate O_2,
697 make it a particularly promising locality for understanding redox structure in a shallow to deep
698 context.

699 **6. Conclusions**

700 The 2.93 Ga Red Lake carbonate platform represents the Earth's earliest known large
701 accumulation of carbonate which preserves evidence for the relationship between shallow and
702 deeper water chemical sedimentary environments in the Mesoarchean Era. The diverse
703 lithofacies associations of the Red Lake carbonate platform suggest variable ocean chemistry and
704 sedimentation processes at the depositional sites.

705 Stromatolitic carbonates dominated the shallow portion of the platform, becoming less
706 important offshore where crystal fan mounds developed, possibly a result of lower light levels in
707 deeper water. Further away from shore, massive calcite layers are separated by magnetite
708 laminae, possibly the result of carbonate whitings in the water column punctuated by upwelling-
709 driven reductions in the degree of carbonate saturation, at the same time providing Fe(II)-rich
710 water on the shelf. Slumped carbonate deposits separate the carbonate inner shelf from iron
711 formation and carbonaceous slate. In slightly deeper water, O_2 generated by photosynthesis in the
712 warm waters of the photic zone likely caused the precipitation of iron hydroxide, manganese
713 oxide and cerium oxide forming the offshore iron formations. The precipitation of chert or
714 magnetite depended on changes in the saturation of seawater with respect to Fe(II) and silicic
715 acid. During periods of low to nil precipitation of chemical sediments, mud accumulated with
716 varying amounts of organic matter. Sediment with higher levels of organics led to strongly
717 reducing conditions developing at the sediment-water interface and possibly overlying water
718 column, precluding the formation or preservation of iron oxides, and led to sulfide mineral
719 precipitation upon Fe oversaturation. Repositioning of the drainage system or storm events
720 periodically brought sand and silt into the area, overwhelming the chemical sedimentary system.

721 The PAAS-normalized REE systematics of carbonate and oxide facies iron formation of
722 Red Lake have several characteristics similar to modern seawater, including suprachondritic

723 Y/Ho ratios, positive La and Gd anomalies, and enrichment of HREEs relative to LREEs, but
724 differ from modern seawater with a general absence of negative Ce anomalies and positive Eu
725 anomalies due to more important hydrothermal inputs to the Mesoarchean ocean relative today.
726 The high Mn concentration (mean 1.3 wt.%) and positive Ce anomalies in the iron formation
727 directly below the carbonate platform as well as the enrichment of redox-sensitive elements in
728 the chemical sedimentary rocks indicate the presence of some O_2 in the depositional sites.
729 Overall, this work portrays a detailed picture of Mesoarchean deeper water facies experiencing
730 water column compositional changes driving a complex interplay of diverse chemical
731 sedimentation processes.

732

733

734

735

736

737

738

739

740 **Acknowledgments**

741 This research was supported by Lakehead University and the European Union's Horizon
742 2020 research and innovation program (grant agreement no. 716515). We thank Goldcorp, Inc
743 for their generous donation of the drill core material, Sean Timpa, Sophie Kurucz, Teegan Ojala,
744 Brittany Ramsay and the rest of the EARTHBLOOM team for their assistance with the cores and
745 in the field, as well as two anonymous reviewers for their detailed reviews. We are also grateful
746 to the editors - Dr. Frances Westall and Dr. Luke Beranek for the constructive feedback and
747 valuable editorial guidance that helped us improve the final manuscript.

748 **References**

749 Albut, G., Babechuk, M.G., Kleinhanns, I.C., Benger, M., Beukes, N.J., Steinhilber, B., Smith,
750 A.J.B., Kruger, S.J., Schoenberg, R., 2018. Modern rather than Mesoarchaean oxidative
751 weathering responsible for the heavy stable Cr isotopic signatures of the 2.95 Ga old
752 Ijzermijn iron formation (South Africa). Geochim. Cosmochim. Acta 228, 157–189.

753 Albut, G., Kamber, B.S., Brüske, A., Beukes, N.J., Smith, A.J.B., Schoenberg, R., 2019. Modern
754 weathering in outcrop samples versus ancient paleoredox information in drill core samples
755 from a Mesoarchaean marine oxygen oasis in Pongola Supergroup, South Africa. Geochim.
756 Cosmochim. Acta 265, 330–353. https://doi.org/https://doi.org/10.1016/j.gca.2019.09.001

757 Allwood, A.C., Kamber, B.S., Walter, M.R., Burch, I.W., Kanik, I., 2010. Trace elements record
758 depositional history of an Early Archean stromatolitic carbonate platform. Chem. Geol. 270,
759 148–163. https://doi.org/10.1016/j.chemgeo.2009.11.013

760 Allwood, A.C., Walter, M.R., Kamber, B.S., Marshall, C.P., Burch, I.W., 2006. Stromatolite reef
761 from the Early Archaean era of Australia. Nature 441, 714–718.
762 https://doi.org/10.1038/nature04764

763 Anbar, A.D., 2007. A Whiff of Oxygen Before the Great Oxidation Event? Science (80-.). 307,
764 111–113.

765 Barrett, T.J., Fralick, P.W., Jarvis, I., 1988. Rare-earth-element geochemistry of some Archean
766 iron formations north of Lake Superior, Ontario. Can. J. Earth Sci. 25, 570–580.

767 Bau, M., Dulski, P., 1996a. Distribution of yttrium and rare-earth elements in the Penge and
768 Kuruman iron-formations, Transvaal Supergroup, South Africa. Precambrian Res. 79, 37–
769 55. https://doi.org/https://doi.org/10.1016/0301-9268(95)00087-9

770 Bau, M., Dulski, P., 1996b. Anthropogenic origin of positive gadolinium anomalies in river

771 waters. Earth Planet. Sci. Lett. 143, 245–255. https://doi.org/10.1016/0012-821X(96)00127-
772 6
773 Bau, M., Dulski, P., 1995. Comparative study of yttrium and rare-earth element behaviours in
774 fluorine-rich hydrothermal fluids. Contrib. to Mineral. Petrol. 119, 213–223.
775 https://doi.org/10.1007/BF00307282
776 Bau, M., Koschinsky, A., Dulski, P., Hein, J.R., 1996. Comparison of the partitioning behaviours
777 of yttrium, rare earth elements, and titanium between hydrogenetic marine ferromanganese
778 crusts and seawater. Geochim. Cosmochim. Acta 60, 1709–1725.
779 Bau, M., Möller, P., 1993. Rare earth element systematics of the chemically precipitated
780 component in early precambrian iron formations and the evolution of the terrestrial
781 atmosphere-hydrosphere-lithosphere system. Geochim. Cosmochim. Acta 57, 2239–2249.
782 https://doi.org/https://doi.org/10.1016/0016-7037(93)90566-F
783 Bekker, A., Slack, J.F., Planavsky, N., Krapež, B., Hofmann, A., Konhauser, K.O., Rouxel, O.J.,
784 2010. Iron formation: The sedimentary product of a complex interplay among mantle,
785 tectonic, oceanic, and biospheric processes. Econ. Geol. 105, 467–508.
786 https://doi.org/10.2113/gsecongeo.105.3.467
787 Beukes, N.J., 1987. Facies relations, depositional environments and diagenesis in a major early
788 Proterozoic stromatolitic carbonate platform to basinal sequence, Campbellrand Subgroup,
789 Transvaal Supergroup, Southern Africa. Sediment. Geol. 54, 1–46.
790 Beukes, N.J., Lowe, D.R., 1989. Environmental control on diverse stromatolite morphologies in
791 the 3000 Myr Pongola Supergroup, South Africa. Sedimentology 36, 383–397.
792 Bolhar, R., Kamber, B.S., Moorbath, S., Fedo, C.M., Whitehouse, M.J., 2004. Characterisation
793 of early Archaean chemical sediments by trace element signatures. Earth Planet. Sci. Lett.

222, 43–60. https://doi.org/10.1016/j.epsl.2004.02.016

Bolhar, R., Van Kranendonk, M.J., 2007. A non-marine depositional setting for the northern Fortescue Group, Pilbara Craton, inferred from trace element geochemistry of stromatolitic carbonates. Precambrian Res. 155, 229–250. https://doi.org/10.1016/j.precamres.2007.02.002

Bolhar, R., Van Kranendonk, M.J., Kamber, B.S., 2005. A trace element study of siderite-jasper banded iron formation in the 3.45 Ga Warrawoona Group, Pilbara Craton - Formation from hydrothermal fluids and shallow seawater. Precambrian Res. 137, 93–114. https://doi.org/10.1016/j.precamres.2005.02.001

Calvert, S.E., Pedersen, T.F., 1993. Geochemistry of Recent oxic and anoxic marine sediments: Implications for the geological record. Mar. Geol. 113, 67–88. https://doi.org/https://doi.org/10.1016/0025-3227(93)90150-T

Card, K.D., Ciesielski, A., 1986. Subdivisions of the Superior Province of the Canadian Shield. Geosci. Canada 13, 5–13.

Cloud, P., 1973. Paleoecological significance of the banded iron-formation. Econ. Geol. 68, 1135–1143. https://doi.org/10.2113/gsecongeo.68.7.1135

Corfu, F., Wallace, H., 1986. U–Pb zircon ages for magmatism in the Red Lake greenstone belt, northwestern Ontario. Can. J. Earth Sci. 23, 27–42. https://doi.org/10.1139/e86-004

Crowe, S.A., Døssing, L.N., Beukes, N.J., Bau, M., Kruger, S.J., Frei, R., Canfield, D.E., 2013. Atmospheric oxygenation three billion years ago. Nature 501, 535–538. https://doi.org/10.1038/nature12426

Danielson, A., Möller, P., Dulski, P., 1992. The europium anomalies in banded iron formations and the thermal history of the oceanic crust. Chem. Geol. 97, 89–100.

https://doi.org/https://doi.org/10.1016/0009-2541(92)90137-T

Delvigne, C., 2012. The Archaean silicon cycle - Insights from silicon isotopes and Ge/Si ratios in banded iron formations, palaeosols and shales. Doctoral thesis. Université libre de Bruxelles, Brussels.

Derry, L.A., Jacobsen, S.B., 1990. The chemical evolution of Precambrian seawater: Evidence from REEs in banded iron formations. Geochim. Cosmochim. Acta 54, 2965–2977. https://doi.org/https://doi.org/10.1016/0016-7037(90)90114-Z

Eickmann, B., Hofmann, A., Wille, M., Bui, T.H., Wing, B.A., Schoenberg, R., 2018. Isotopic evidence for oxygenated Mesoarchaean shallow oceans. Nat. Geosci. 11, 133–138. https://doi.org/10.1038/s41561-017-0036-x

Elderfield, H., 1988. The oceanic chemistry of the rare-earth elements. Philos. Trans. R. Soc. London. Ser. A, Math. Phys. Sci. 325, 105–126.

Elderfield, H., Greaves, M.J., 1982. The rare earth elements in seawater. Nature 296, 214–219. https://doi.org/10.1038/296214a0

Eroglu, S., van Zuilen, M.A., Taubald, H., Drost, K., Wille, M., Swanner, E.D., Beukes, N.J., Schoenberg, R., 2017. Depth-dependent δ13C trends in platform and slope settings of the Campbellrand-Malmani carbonate platform and possible implications for Early Earth oxygenation. Precambrian Res. 302, 122–139.

Fowler, A.D., Doig, R., 1983. The significance of europium anomalies in the REE spectra of granites and pegmatites, Mont Laurier, Quebec. Geochim. Cosmochim. Acta 47, 1131–1137.

Fralick, P., Riding, R., 2015. Steep Rock Lake: Sedimentology and geochemistry of an Archean carbonate platform. Earth-Science Rev. 151, 132–175.

https://doi.org/10.1016/j.earscirev.2015.10.006

Fralick, P.W., Barrett, T.J., Jarvis, K.E., Jarvis, I., Schnieders, B.R., Kemp, R. Vande, 1989. Sulfide-facies iron formation at the Archean Morley occurrence, northwestern Ontario. Contrasts with oceanic hydrothermal deposits. Can. Mineral. 27 pt 4, 601–616.

Fralick, P.W., Hollings, P., King, D., 2008. Stratigraphy, geochemistry and depositional environments of Mesoarchean sedimentary units in Western Superior Province: implications for generation of early crust. When did plate tectonics begin planet Earth 77–96.

Frei, R., Gaucher, C., Poulton, S.W., Canfield, D.E., 2009. Fluctuations in Precambrian atmospheric oxygenation recorded by chromium isotopes. Nature 461, 250–253. https://doi.org/10.1038/nature08266

Gauthier-Lafaye, F., Weber, F., 2003. Natural nuclear fission reactors: time constraints for occurrence, and their relation to uranium and manganese deposits and to the evolution of the atmosphere. Precambrian Res. 120, 81–100. https://doi.org/https://doi.org/10.1016/S0301-9268(02)00163-8

Goldberg, E.D., Koide, M., Schmitt, R.A., Smith, R.H., 1963. Rare-Earth distributions in the marine environment. J. Geophys. Res. 68, 4209–4217. https://doi.org/10.1029/JZ068i014p04209

Goodwin, A.M., 1973. Archean Iron-Formations and Tectonic basins of the Canadian Shield. Econ. Geol. 68, 915–933.

Gregory, D., Mukherjee, I., Olson, S.L., Large, R.R., Danyushevsky, L. V, Stepanov, A.S., Avila, J.N., Cliff, J., Ireland, T.R., Raiswell, R., Olin, P.H., Maslennikov, V. V, Lyons, T.W., 2019. The formation mechanisms of sedimentary pyrite nodules determined by trace

863 element and sulfur isotope microanalysis. Geochim. Cosmochim. Acta 259, 53–68.
864 https://doi.org/https://doi.org/10.1016/j.gca.2019.05.035
865 Gross, G.A., Zajac, I.S., 1983. Iron-Formation in Fold Belts Marginal to the Ungava Craton, in:
866 Trendall, A.F., Morris, R.C.B.T.-D. in P.G. (Eds.), Iron-Formation Facts and Problems.
867 Elsevier, pp. 253–294. https://doi.org/https://doi.org/10.1016/S0166-2635(08)70045-8
868 Grotzinger, J.P., 1989. Facies and evolution of Precambrian carbonate depositional systems:
869 emergence of the modern platform archetype. Control. carbonate Platf. basin Dev. 71–106.
870 Hofmann, A., 2011. Archaean hydrothermal systems in the Barberton greenstone belt and their
871 significance as a habitat for early life, in: Earliest Life on Earth: Habitats, Environments and
872 Methods of Detection. Springer, pp. 51–78.
873 Hofmann, H.J., Thurston, P.C., Wallace, H., 1985. Archean stromatolites from Uchi greenstone
874 belt, northwestern Ontario, in: Evolution of Archean Supracrustal Sequences. Geol. Assoc.
875 Can. Spec. Pap., pp. 125–132.
876 Holland, H.D., 1974. Aspects of the Geologic History of Seawater BT - Cosmochemical
877 Evolution and the Origins of Life, in: Oró, J., Miller, S.L., Ponnamperuma, C., Young, R.S.
878 (Eds.), . Springer Netherlands, Dordrecht, pp. 87–91.
879 Holland, H.D., 1973. The Oceans: A possible source of iron in iron-formations. Econ. Geol. 68,
880 1169–1172. https://doi.org/10.2113/gsecongeo.68.7.1169
881 Hollings, P., Wyman, D., Kerrich, R., 1999. Komatiite–basalt–rhyolite volcanic associations in
882 Northern Superior Province greenstone belts: significance of plume-arc interaction in the
883 generation of the proto continental Superior Province. Lithos 46, 137–161.
884 https://doi.org/10.1016/S0024-4937(98)00058-9
885 Hollings, P.N., 1999. Geochemistry in the Uchi subprovince, northern Superior Province: an

886 evaluation of the geodynamic evolution of the northern margin of the Superior Province
887 ocean basin.
888 Kamber, B.S., Webb, G.E., 2001. The geochemistry of late Archaean microbial carbonate:
889 Implications for ocean chemistry and continental erosion history. Geochim. Cosmochim.
890 Acta 65, 2509–2525. https://doi.org/10.1016/S0016-7037(01)00613-5
891 Klein, C., Beukes, N.J., 1989. Geochemistry and Sedimentology of a Facies Transition from
892 Limestone to Iron-Formation Deposition in the Early Proterozoic Transvaal Supergroup,
893 South-Africa. Econ. Geol. 84, 1733–1774.
894 Klinkhammer, G., Elderfield, H., Hudson, A., 1983. Rare earth elements in seawater near
895 hydrothermal vents. Nature 305, 185–188.
896 Klinkhammer, G.P., Elderfield, H., Edmond, J.M., Mitra, A., 1994. Geochemical implications of
897 rare earth element patterns in hydrothermal fluids from mid-ocean ridges. Geochim.
898 Cosmochim. Acta 58, 5105–5113.
899 Knoll, A.H., Beukes, N.J., 2009. Introduction: Initial investigations of a Neoarchean shelf
900 margin-basin transition (Transvaal Supergroup, South Africa). Precambrian Res. 169, 1–14.
901 https://doi.org/https://doi.org/10.1016/j.precamres.2008.10.009
902 Konhauser, K.O., Lalonde, S. V, Planavsky, N.J., Pecoits, E., Lyons, T.W., Mojzsis, S.J.,
903 Rouxel, O.J., Barley, M.E., Rosìere, C., Fralick, P.W., Kump, L.R., Bekker, A., 2011.
904 Aerobic bacterial pyrite oxidation and acid rock drainage during the Great Oxidation Event.
905 Nature 478, 369–73. https://doi.org/10.1038/nature10511
906 Lalonde, S. V., Konhauser, K.O., 2015. Benthic perspective on Earth's oldest evidence for
907 oxygenic photosynthesis. Proc. Natl. Acad. Sci. 112.
908 https://doi.org/10.1073/pnas.1415718112

909 Lowe, D.R., Knauth, L.P., 1977. Sedimentology of the Onverwacht Group (3.4 billion years),
910 Transvaal, South Africa, and its bearing on the characteristics and evolution of the early
911 earth. J. Geol. 85, 699–723.
912 Maliva, R.G., Knoll, A.H., Simonson, B.M., 2005. Secular change in the Precambrian silica
913 cycle: Insights from chert petrology. GSA Bull. 117, 835–845.
914 Mason, T.R., Von Brunn, V., 1977. 3-Gyr-old stromatolites from South Africa. Nature 266, 47–
915 49.
916 McIntyre, T., Fralick, P., 2017. Sedimentology and Geochemistry of the 2930 Ma Red Lake-
917 Wallace Lake Carbonate Platform, Western Superior Province, Canada. Depos. Rec. 3,
918 258–287. https://doi.org/10.1002/dep2.36
919 Meyer, K.M., Kump, L.R., 2008. Oceanic euxinia in Earth history: causes and consequences.
920 Annu. Rev. Earth Planet. Sci. 36, 251–288.
921 Morford, J.L., Russell, A.D., Emerson, S., 2001. Trace metal evidence for changes in the redox
922 environment associated with the transition from terrigenous clay to diatomaceous sediment,
923 Saanich Inlet, BC. Mar. Geol. 174, 355–369. https://doi.org/https://doi.org/10.1016/S0025-
924 3227(00)00160-2
925 Mortlock, R.A., Froelich, P.N., Feely, R.A., Massoth, G.J., Butterfield, D.A., Lupton, J.E., 1993.
926 Silica and germanium in Pacific Ocean hydrothermal vents and plumes. Earth Planet. Sci.
927 Lett. 119, 365–378. https://doi.org/https://doi.org/10.1016/0012-821X(93)90144-X
928 Nozaki, Y., Zhang, J., Amakawa, H., 1997. The fractionation between Y and Ho in the marine
929 environment. Earth Planet. Sci. Lett. 148, 329–340. https://doi.org/10.1016/S0012-
930 821X(97)00034-4
931 Olson, S.L., Kump, L.R., Kasting, J.F., 2013. Quantifying the areal extent and dissolved oxygen

concentrations of Archean oxygen oases. Chem. Geol. 362, 35–43.

Ossa Ossa, F., Hofmann, A., Vidal, O., Kramers, J.D., Belyanin, G., Cavalazzi, B., 2016. Unusual manganese enrichment in the Mesoarchean Mozaan Group, Pongola Supergroup, South Africa. Precambrian Res. 281, 414–433. https://doi.org/https://doi.org/10.1016/j.precamres.2016.06.009

Peter, J., 2003. Ancient iron-rich metalliferous sediments (iron formations): their genesis and use in the exploration for stratiform... Geochemistry sediment Sediment. rocks 1145–176.

Pirie, J., 1981. Regional setting of gold deposits in the Red Lake area, northwestern Ontario; in Genesis of Archean volcanic-hosted gold deposits; Ontario Geological Survey, Miscellaneous Paper 97, 71–93.

Planavsky, N., Bekker, A., Rouxel, O.J., Kamber, B., Hofmann, A., Knudsen, A., Lyons, T.W., 2010. Rare Earth Element and yttrium compositions of Archean and Paleoproterozoic Fe formations revisited: New perspectives on the significance and mechanisms of deposition. Geochim. Cosmochim. Acta 74, 6387–6405. https://doi.org/10.1016/j.gca.2010.07.021

Planavsky, N.J., Asael, D., Hofmann, A., Reinhard, C.T., Lalonde, S. V, Knudsen, A., Wang, X., Ossa Ossa, F., Pecoits, E., Smith, A.J.B., Beukes, N.J., Bekker, A., Johnson, T.M., Konhauser, K.O., Lyons, T.W., Rouxel, O.J., 2014. Evidence for oxygenic photosynthesis half a billion years before the Great Oxidation Event. Nat. Geosci. 7, 283–286. https://doi.org/10.1038/ngeo2122

Poulton, S.W., Fralick, P.W., Canfield, D.E., 2010. Spatial variability in oceanic redox structure 1.8 billion years ago. Nat. Geosci. 3, 486–490. https://doi.org/10.1038/ngeo889

Pufahl, P.K., Fralick, P.W., 2004. Depositional controls on Palaeoproterozoic iron formation accumulation, Gogebic Range, Lake Superior region, USA. Sedimentology 51, 791–808.

955 Riding, R., Fralick, P., Liang, L., 2014. Identification of an Archean marine oxygen oasis.
956 Precambrian Res. 251, 232–237. https://doi.org/10.1016/j.precamres.2014.06.017
957 Robbins, L.J., Lalonde, S. V, Planavsky, N.J., Partin, C.A., Reinhard, C.T., Kendall, B., Scott,
958 C., Hardisty, D.S., Gill, B.C., Alessi, D.S., Dupont, C.L., Saito, M.A., Crowe, S.A.,
959 Poulton, S.W., Bekker, A., Lyons, T.W., Konhauser, K.O., 2016. Trace elements at the
960 intersection of marine biological and geochemical evolution. Earth-Science Rev. 163, 323–
961 348. https://doi.org/https://doi.org/10.1016/j.earscirev.2016.10.013
962 Rosing, M.T., Frei, R., 2004. U-rich Archaean sea-floor sediments from Greenland – indications
963 of >3700 Ma oxygenic photosynthesis. Earth Planet. Sci. Lett. 217, 237–244.
964 https://doi.org/https://doi.org/10.1016/S0012-821X(03)00609-5
965 Roy, S., 2006. Sedimentary manganese metallogenesis in response to the evolution of the Earth
966 system. Earth-Science Rev. 77, 273–305.
967 https://doi.org/https://doi.org/10.1016/j.earscirev.2006.03.004
968 Russell, A.D., Morford, J.L., 2001. The behavior of redox-sensitive metals across a laminated–
969 massive–laminated transition in Saanich Inlet, British Columbia. Mar. Geol. 174, 341–354.
970 https://doi.org/https://doi.org/10.1016/S0025-3227(00)00159-6
971 Sahoo, S.K., Planavsky, N.J., Kendall, B., Wang, X., Shi, X., Scott, C., Anbar, A.D., Lyons,
972 T.W., Jiang, G., 2012. Ocean oxygenation in the wake of the Marinoan glaciation. Nature
973 489, 546–549.
974 Sanborn-Barrie, M., Skulski, T., Parker, J., Dubé, B., 2000. Integrated regional analysis of the
975 Red Lake greenstone belt and its mineral deposits , western Superior Province , Ontario.
976 Geol. Surv. Canada Current Re, 14.
977 Sanborn-Barrie, M., Skulski, T., Parker, J.R., 2004. Geology, Red Lake greenstone belt, western

978 Superior province, Ontario: Gelogical Survey of Canada Open File 4594, 1:50,000 scale
979 color map. https://doi.org/10.4095/215464
980 Sanborn-Barrie, M., Skulski, T., Parker, J.R., 2001. Three hundred million years of tectonic
981 history recorded by the Red Lake greenstone belt, Ontario. Geol. Surv. Canada Current Re,
982 14. https://doi.org/10.4095/212109
983 Shibuya, T., Komiya, T., Nakamura, K., Takai, K., Maruyama, S., 2010. Highly alkaline, high-
984 temperature hydrothermal fluids in the early Archean ocean. Precambrian Res. 182, 230–
985 238. https://doi.org/https://doi.org/10.1016/j.precamres.2010.08.011
986 Shields, G., Stille, P., 2001. Diagenetic constraints on the use of cerium anomalies as
987 palaeoseawater redox proxies: an isotopic and REE study of Cambrian phosphorites. Chem.
988 Geol. 175, 29–48. https://doi.org/https://doi.org/10.1016/S0009-2541(00)00362-4
989 Sholkovitz, E.R., Landing, W.M., Lewis, B.L., 1994. Ocean particle chemistry: The fractionation
990 of rare earth elements between suspended particles and seawater. Geochim. Cosmochim.
991 Acta 58, 1567–1579. https://doi.org/https://doi.org/10.1016/0016-7037(94)90559-2
992 Siahi, M., Hofmann, A., Hegner, E., Master, S., 2016. Sedimentology and facies analysis of
993 Mesoarchaean stromatolitic carbonate rocks of the Pongola Supergroup, South Africa.
994 Precambrian Res. 278, 244–264.
995 https://doi.org/https://doi.org/10.1016/j.precamres.2016.03.004
996 Siahi, M., Hofmann, A., Master, S., Wilson, A., Mayr, C., 2018. Trace element and stable (C, O)
997 and radiogenic (Sr) isotope geochemistry of stromatolitic carbonate rocks of the
998 Mesoarchaean Pongola Supergroup: Implications for seawater composition. Chem. Geol.
999 476, 389–406.
1000 Siever, R., 1992. The silica cycle in the Precambrian. Geochim. Cosmochim. Acta 56, 3265–

1001 3272. https://doi.org/https://doi.org/10.1016/0016-7037(92)90303-Z
1002 Siever, R., 1957. The Silica Budget in the Sedimentary Cycle. Am. Mineral. 42, 821–841.
1003 Smith, A.J.B., Beukes, N.J., Gutzmer, J., Johnson, C.M., Czaja, A.D., Nhleko, N., de Beer, F.,
1004 Hoffman, J.W., Awramik, S.M., 2020. Life on a Mesoarchean marine shelf–insights from
1005 the world's oldest known granular iron formation. Sci. Rep. 10, 1–8.
1006 Sumner, D.Y., 1996. Evidence for low late Archean atmospheric oxygen from oceanic depth
1007 gradients in iron concentration. Geol. Soc. Am. Bull. 28, 218.
1008 Sumner, D.Y., Grotzinger, J.P., 1996. Were kinetics of Archean calcium carbonate precipitation
1009 related to oxygen concentration? Geology 24, 119–122. https://doi.org/10.1130/0091-
1010 7613(1996)024<0119:WKOACC>2.3.CO;2
1011 Takahashi, Y., Sakami, H., Nomura, M., 2002. Determination of the oxidation state of cerium in
1012 rocks by Ce LIII-edge X-ray absorption near-edge structure spectroscopy. Anal. Chim. Acta
1013 468, 345–354.
1014 Taylor, S.R., McLennan, S.M., 1985. The continental crust: its composition and evolution.
1015 Blackwell Scientific Pub., Palo Alto, CA.
1016 Thoby, M., Konhauser, K.O., Fralick, P.W., Altermann, W., Visscher, P.T., Lalonde, S. V, 2019.
1017 Global importance of oxic molybdenum sinks prior to 2 . 6 Ga revealed by the Mo isotope
1018 composition of Precambrian carbonates 47, 559–562.
1019 Thurston, P.C., Breaks, F.W., 1978. Metamorphic and tectonic evolution of the Uchi-English
1020 River Subprovince, in: Metamorphism in the Canadian Shield. pp. 49–62.
1021 Tostevin, R., Shields, G.A., Tarbuck, G.M., He, T., Clarkson, M.O., Wood, R.A., 2016a.
1022 Effective use of cerium anomalies as a redox proxy in carbonate-dominated marine settings.
1023 Chem. Geol. 438, 146–162. https://doi.org/https://doi.org/10.1016/j.chemgeo.2016.06.027

1024 Tostevin, R., Wood, R.A., Shields, G.A., Poulton, S.W., Guilbaud, R., Bowyer, F., Penny, A.M.,
1025 He, T., Curtis, A., Hoffmann, K.H., 2016b. Low-oxygen waters limited habitable space for
1026 early animals. Nat. Commun. 7, 1–9.
1027 Tsikos, H., Matthews, A., Erel, Y., Moore, J.M., 2010. Iron isotopes constrain biogeochemical
1028 redox cycling of iron and manganese in a Palaeoproterozoic stratified basin. Earth Planet.
1029 Sci. Lett. 298, 125–134. https://doi.org/https://doi.org/10.1016/j.epsl.2010.07.032
1030 Van den Boorn, S., 2008. Silicon isotopes and the origin of the Archaean cherts. Geologica
1031 Ultraiectina (293). Departement Aardwetenschappen.
1032 Van Kranendonk, M.J., 2006. Volcanic degassing, hydrothermal circulation and the flourishing
1033 of early life on Earth: A review of the evidence from c. 3490-3240 Ma rocks of the Pilbara
1034 Supergroup, Pilbara Craton, Western Australia. Earth-Science Rev. 74, 197–240.
1035 https://doi.org/https://doi.org/10.1016/j.earscirev.2005.09.005
1036 Van Kranendonk, M.J., Webb, G.E., Kamber, B.S., 2003. Geological and trace element evidence
1037 for a marine sedimentary environment of deposition and biogenicity of 3.45 Ga
1038 stromatolitic carbonates in the Pilbara Craton, and support for a reducing Archaean ocean.
1039 Geobiology 1, 91–108.
1040 Voegelin, A.R., Nägler, T.F., Beukes, N.J., Lacassie, J.P., 2010. Molybdenum isotopes in late
1041 Archean carbonate rocks: Implications for early Earth oxygenation. Precambrian Res. 182,
1042 70–82. https://doi.org/https://doi.org/10.1016/j.precamres.2010.07.001
1043 Wang, J., Chen, D., Wand, D., Yan, D., Zhou, X., Wang, Q., 2011. Petrology and geochemistry
1044 of chert on the marginal zone of Yangtze Platform, western Hunan, South China, during the
1045 Ediacaran–Cambrian transition. Sedimentology 59, 809–829.
1046 https://doi.org/10.1111/j.1365-3091.2011.01280.x

1047 Webb, G.E., Kamber, B.S., 2000. Rare earth elements in Holocene reefal microbialites: A new
1048 shallow seawater proxy. Geochim. Cosmochim. Acta 64, 1557–1565.
1049 https://doi.org/10.1016/S0016-7037(99)00400-7
1050 Wedepohl, K.H., 1991. The composition of the primitive upper earth's mantle, in: International
1051 Kimberlite Conference: Extended Abstracts. pp. 451–453.
1052 Wedepohl, K.H., 1971. Environmental influences on the chemical composition of shales and
1053 clays. Phys. Chem. Earth 8, 307–333.
1054 Wille, M., Nebel, O., Van Kranendonk, M.J., Schoenberg, R., Kleinhanns, I.C., Ellwood, M.J.,
1055 2013. Mo–Cr isotope evidence for a reducing Archean atmosphere in 3.46–2.76 Ga black
1056 shales from the Pilbara, Western Australia. Chem. Geol. 340, 68–76.
1057 Wright, D.T., Altermann, W., 2000. Microfacies development in Late Archaean stromatolites
1058 and oolites of the Ghaap Group of South Africa. Geol. Soc. London, Spec. Publ. 178, 51–
1059 70.
1060 Zhang, J., Nozaki, Y., 1996. Rare earth elements and yttrium in seawater: ICP-MS
1061 determinations in the East Caroline, Coral Sea, and South Fiji basins of the western South
1062 Pacific Ocean. Geochim. Cosmochim. Acta 60, 4631–4644.
1063 Zhao, K.-D., Jiang, S.-Y., 2007. Rare earth element and yttrium analyses of sulfides from the
1064 Dachang Sn-polymetallic ore field, Guangxi Province, China: Implication for ore genesis.
1065 Geochem. J. 41, 121–134.
1066
1067
1068
1069

1070 **Figure Captions**

1071 Figure 1. Location of the Red Lake Greenstone Belt, as indicated by the red square, (A) in the
1072 Canadian Shield and (B) within the Uchi Subprovince, Superior Province, Canada (modified
1073 after Card and Ciesielski, 1986). (C) Stratigraphy of the Ball assemblages (modified after
1074 Hollings, 1999) containing the Red Lake carbonate platform in relation to the Red Lake
1075 Greenstone Belt. (D) Geological map of the Red Lake carbonate platform and accompanying
1076 igneous and sedimentary rocks in the Red Lake Greenstone Belt (modified after Sanborn-Barrie
1077 et al., 2004).

1078 Figure 2. The stratigraphic correlation of the nine drill holes core shows alternating deposition of
1079 chemical and siliciclastic sedimentary rocks, with shallow water stromatolitic carbonate
1080 overlying and underlying the deeper water rocks. The lateral spacing of the stratigraphic columns
1081 on the figure represents the approximate relative position of their drill collars from west to east.
1082 The inset (green box, top right corner) shows the stratigraphic section of the transitional facies
1083 which are preserved approximately 4 km east of the NGI10-31 hole in the Hall Bay area (outcrop
1084 4 in Figure 1D). The correlation panel between the PB12-35 and the PB12-34 holes and the
1085 PB12-32 and the NGI10-31 holes represents the A to A′ and B to B′ lines, respectively, as
1086 depicted in Figure 1D.

1087 Figure 3. (A) Carbonate-magnetite facies present on the shoreline of Hall Bay (outcrop - 4 in
1088 Figure 1D). White, cm-scale calcite layers alternate with mm-scale magnetite laminae. Contacts
1089 are generally sharp with low amounts of magnetite in the carbonate layers. (B) Polished slab
1090 displaying mm-thick magnetite-rich laminae with some sharp contacts (white arrow) and others
1091 that grade up through a more diffuse mixture of magnetite and calcite to more pure calcite (black

1092 arrow). (C) The thin section under XPL shows inequigranular, fine to coarse crystalline calcite
1093 grains with xenotopic fabric. Calcite recrystallization has obliterated primary textures. The
1094 carbonate matrix in the recrystallized magnetite layers consists of linear strands of small crystals
1095 which are probably secondary.

1096 Figure 4. μXRF elemental maps with false-color images showing: (A) Carbonate-magnetite with
1097 cm-scale calcite layers interlayered with mm-scale magnetite laminae, which in places grade
1098 upwards into calcite. Cavities between calcite layers are filled with calcite cement and secondary
1099 silica cement (white arrows in 4A-i and 4A-iii, respectively); (B) A carbonate sample show mass
1100 flow features, where carbonate clasts are clast-supported in the lower layer and matrix-supported
1101 in the upper layer. The matrix is calcite mixed with magnetite and siliciclastics.

1102 Figure 5. Field photographs showing features of the transitional facies: (A) Slumped carbonate
1103 on the shoreline of Hall Bay at outcrop 4 in Figure 1D; (B) Dispersed, contorted carbonate clasts
1104 in a carbonaceous mudstone matrix; (C) Clast-supported elongated cherty carbonate clasts and
1105 convoluted layers overlie matrix-supported clasts in carbonaceous mudstone; (D) Carbonate
1106 mass flow with scattered, sub-rounded to sub-angular carbonate clasts embedded in
1107 carbonaceous mudstone. Near the bottom, carbonate laminae are somewhat preserved and have a
1108 sharp contact with an underlying 2.5 cm thick magnetite layer.

1109 Figure 6. Photographs showing features of the offshore oxide facies iron formation: (A) Straight
1110 and parallel magnetite bands of 2 to 5 cm thickness interbedded with chert bands of similar
1111 thickness with sharp contacts (outcrop 1 in Figure 1D). The pencil magnet is 12.3 cm; B)
1112 Massive chert beds of 15 to 20 cm in thickness alternate with thin magnetite laminae ~5 cm in
1113 thickness (outcrop 3 in Figure 1D). The assemblage has a sharp upper contact with sulfidic slate

1114 (top of the photograph of Figure 7A); C) Polished core showing parallel, straight, white to
1115 greyish-white chert bands of variable thickness alternating with magnetite bands. The yellowish-
1116 brown lining at the contact of chert and magnetite is grunerite. The core is 4.6 cm thick, and the
1117 sample is taken from the EBL10-27 hole.

1118 Figure 7. Photographs showing features of the offshore sulfidic slate facies: (A) Heavily
1119 weathered, rusty iron sulfide-rich slate in contact with chert containing thin magnetite layers
1120 (outcrop 3 in Figure 1D); (B) Pyrite nodules 0.5 cm to 1 cm in diameter are present in the
1121 outcrop near the east side of Bridget Lake (outcrop 1 in Figure 1D). Polished core slabs (4.6 cm
1122 thick) of sulfidic slate taken from the PB12- 32 and EBL10-27 holes, respectively; (C) Pyrite
1123 nodules >1 cm in diameter scattered in a carbonaceous slate matrix; (D) Crenulated pyrite
1124 lamination of mm-scale embedded in carbonaceous slate; (E) SEM-EDS mineral map showing
1125 recrystallized euhedral pyrite (Py) in contact with anhedral pyrrhotite (Po) and demonstrating the
1126 co-occurrence of these two minerals in the sulfidic slates.

1127 Figure 8. The redox-sensitive elements Cr, Mo, V, and U are plotted against oxides of elements
1128 (Al_2O_3 and TiO_2) that are chemically immobile under normal weathering and sediment transport
1129 conditions. The samples show an overall positive linear correlation in the cross-plots of Al_2O_3
1130 and TiO_2 vs. Cr, Mo, V, and U, but the redox-sensitive element-enriched samples deviate from
1131 the linear correlation. For example, in (A) and (B), Cr is showing enrichment in the carbonate
1132 fraction, (C) and (D) show that Mo is enriched in most of the chemical sediments, (E) and (F) V
1133 is enriched in the iron formation, and (G) and (H) U is enriched in the carbonate.

1134 Figure 9. Enrichment factors (EF) for Cr, Mo, V, and U in iron formation, carbonate, chert,
1135 pyrite, pyrrhotite, and black slate show variable degrees of enrichment of these elements in these

1136 lithologies. Values for EF greater than 1 indicate the enrichment of trace elements relative to
1137 values that would be expected considering only the siliciclastic component of each sample (as
1138 traced by TiO_2; Wedepohl, 1971, 1991); the reference siliciclastic compositions in each plot are
1139 represented by dashed lines at EF=1. (A) The logarithmic plot of enrichment factors for Cr
1140 indicates that some iron formation, pyrite, pyrrhotite, and most of the carbonate samples have Cr
1141 concentrations greater than expected for siliciclastic contributions alone. (B) The Mo enrichment
1142 factor plot shows that most of the chemical sediments have a greater abundance of Mo than
1143 expected for the siliciclastic sources. (C) The enrichment factor plot of V indicates that most of
1144 the iron formation, pyrite, and pyrrhotite samples are enriched in V. (D) U enrichment factors
1145 show a high abundance of U in carbonate samples. Most of the iron formation and chert samples
1146 have moderate authigenic enrichment in U. The enrichment of redox-sensitive elements in the
1147 chemical sediments may indicate mild oxidative weathering, hydrothermal contributions, or
1148 other poorly understood weathering processes driving elemental enrichment in Mesoarchean
1149 seawater.

1150 Figure 10. (A) Plot of Y/Ho ratios vs. Al_2O_3 with dashed lines showing the mass ratio of average
1151 crustal rocks (Y/Ho = 27 g/g) and 1 wt. % Al_2O_3 siliciclastic cutoff for pure chemical sediments,
1152 respectively. Carbonate and magnetite samples with < 1 wt. % Al_2O_3 are scattered on the Y/Ho
1153 axis, plotting mostly above the average slate value of 27, indicating low degrees of siliciclastic
1154 contamination. Most pyrite and pyrrhotite samples, and all black slate samples, plot near the
1155 average shale value, indicating a strong siliciclastic influence. (B) Y/Ho ratio vs. slope of the
1156 PAAS-normalized total REE pattern. The horizontal dashed line represents the Y/Ho mass ratio
1157 of average crustal rocks (27 g/g). The vertical dashed line shows the slope value of 1, where
1158 samples with a slope value >1 indicate depletion in HREE while a slope value <1 shows

1159 depletion in LREE. Most black slate, sulfide, and chert samples have low amounts of light REE
1160 (LREE) depletion or mild LREE enrichment compared to the strong LREE depletion exhibited
1161 by most of the iron formation and carbonate samples.

1162 Figure 11. PAAS-normalized Gd anomaly versus Eu anomaly plot calculated as
1163 Gd/Gd*=Gd/(0.33Sm+0.67Tb) and Eu/Eu* = Eu/(0.67Sm+0.33Tb), respectively (as per Bau et
1164 al., 1996). This plot discriminates between Gd and Eu anomalies. The dashed lines represent
1165 expected values for the absence of Eu and Gd anomalies, whereas $(Eu)_{PAAS} > 1$ and $(Gd)_{PAAS} >$
1166 1 are indicative of positive Eu and Gd anomalies, respectively. The samples roughly fall into
1167 three groups: the carbonates, oxide iron formations and cherts have Eu anomalies comparable to
1168 Archean seawater; the black slate samples generally have lower positive Eu anomalies, and the
1169 isolated sulfides have even smaller Eu anomalies. Two of the iron sulfide samples and one black
1170 slate sample show negative Eu anomalies. Positive Gd anomalies are a common feature of
1171 modern seawater, and all Red Lake samples exhibit this anomaly, further supporting their marine
1172 origin.

1173 Figure 12. PAAS-normalized (Taylor and McLennan, 1985) REE spectra for Red Lake chemical
1174 sedimentary and siliciclastic rocks. The patterns for carbonate and oxide facies iron formation
1175 are similar to each other, as are the patterns for black slate, pyrite, and pyrrhotite. Pyrite and
1176 pyrrhotite were plotted separately to facilitate the comparison of their respective REE patterns.
1177 The omnipresence of Eu anomalies in these rocks indicates that Red Lake seawater was subject
1178 to important hydrothermal influence. (A) and (B) The carbonate and oxide iron formation
1179 samples are depleted in LREE and have pronounced positive Eu anomalies. (C) The chert
1180 samples are enriched in LREE with even more substantial Eu anomalies, which, given the REE-
1181 poor composition of their cherty matrix, may reflect contributions from micro-inclusions of

magnetite and felsic detritus. (D), (E) and (F) The black slate, pyrite, and pyrrhotite samples have flat REE patterns with more mild Eu anomalies.

Figure 13. PAAS-normalized slope of the heavy REE (evaluated as Gd/Yb) vs. slope of total REE (Pr/Yb) with the dashed line marking a slope value of 1. Samples with a slope value of >1 indicate enrichment in LREE while a slope value <1 shows enrichment of HREE. The majority of carbonate and magnetite samples are LREE-depleted, similar to Archean and modern seawater. The black slate, sulfides, and chert are LREE-enriched, similar to the average continental crust.

Figure 14. PAAS-normalized Pr anomaly versus Ce anomaly plot calculated as Ce/Ce* = Ce/(0.5La+0.5Pr) and Pr/Pr* = Pr/(0.5Ce+0.5Nd), respectively (as per Bau and Dulski, 1996a). This plot differentiates between true Ce anomalies and false Ce anomalies arising from anomalies in La. The grey-shaded area represents an absence of true Ce anomalies. One isolated sample shows an apparent true negative Ce anomaly. The black slates and most of the sulfides do not have appreciable La or Ce anomalies, whereas half of the iron formation and several carbonate samples, and all of the chert samples, have positive Ce anomalies indicating that Ce was oxidized in the presence of some oxygen and preferentially precipitated from seawater compared to other REE during the deposition of the iron formations and carbonates.

Figure 15. PAAS-normalized average REE patterns for the main deep water lithologies compared to the shallow water Red Lake stromatolites (data from McIntyre and Fralick, 2017). (A) The shallow water stromatolitic carbonates, deeper water carbonates, and oxide facies iron formation have very similar patterns reflecting Archean seawater. The chert has a distinct pattern with LREE enrichment and positive Eu anomalies. This could be caused by micro-inclusions of

1204 magnetite and felsic detritus. (B) The carbonaceous slate, pyrite, and pyrrhotite have similar
1205 patterns, highlighting the control of inclusions, most likely carbonaceous slate, on sulfide REE
1206 patterns.

1207 Figure 16. (A) SEM-EDS layered false-color image of a carbonate-magnetite sample. The
1208 carbonate band and the iron band are composed of calcite and magnetite, respectively, and
1209 calcite is also present as a matrix in the magnetite band. (B) The elemental map of Al shows mud
1210 lining on both sides of the magnetite band, indicating hiatuses between carbonate and magnetite
1211 precipitation. (C) The elemental map of Si also shows a higher concentration of Si in the
1212 magnetite band.

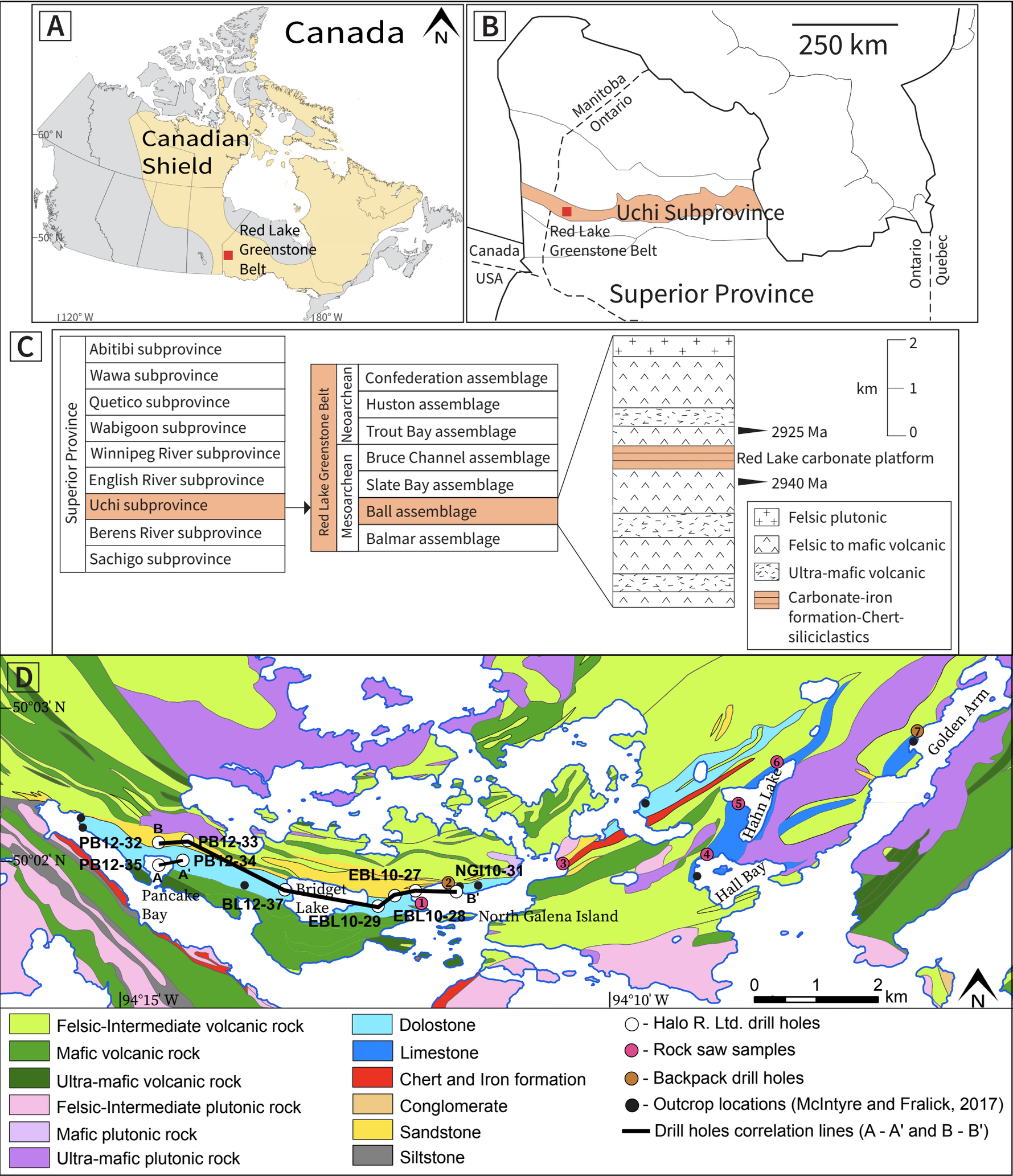
A
Canada
N
Canadian Shield
Red Lake Greenstone Belt
60° N
50° N
120° W
80° W
B
250 km
Manitoba
Ontario
Uchi Subprovince
Red Lake Greenstone Belt
Canada
USA
Superior Province
Ontario
Quebec
C
Superior Province
Abitibi subprovince
Wawa subprovince
Quetico subprovince
Wabigoon subprovince
Winnipeg River subprovince
English River subprovince
Uchi subprovince
Berens River subprovince
Sachigo subprovince
Red Lake Greenstone Belt
Neoarchean
Mesoarchean
Confederation assemblage
Huston assemblage
Trout Bay assemblage
Bruce Channel assemblage
Slate Bay assemblage
Ball assemblage
Balmar assemblage
2925 Ma
Red Lake carbonate platform
2940 Ma
km
2
1
0
Felsic plutonic
Felsic to mafic volcanic
Ultra-mafic volcanic
Carbonate-iron formation-Chert-siliciclastics
D
50°03' N
50°02' N
94°15' W
94°10' W
PB12-32
PB12-33
PB12-35
PB12-34
A
A'
B
B'
Pancake Bay
BL12-37
Bridget Lake
EBL10-29
EBL10-28
EBL10-27
NGI10-31
North Galena Island
Hall Bay
Hahn Lake
Golden Arm
1
2
3
4
5
6
7
0
1
2
km
N
Felsic-Intermediate volcanic rock
Mafic volcanic rock
Ultra-mafic volcanic rock
Felsic-Intermediate plutonic rock
Mafic plutonic rock
Ultra-mafic plutonic rock
Dolostone
Limestone
Chert and Iron formation
Conglomerate
Sandstone
Siltstone
- Halo R. Ltd. drill holes
- Rock saw samples
- Backpack drill holes
- Outcrop locations (McIntyre and Fralick, 2017)
Drill holes correlation lines (A - A' and B - B')

Pancake Bay

A — A′

PB12-34

PB12-35

Shallow water facies	Deeper water facies	Volcanic rock
Dolostone	Limestone	Basalt
Conglomerate	Oxide Iron Formation	Komatiite
Sandstone	Chert	Stromatolite
Siltstone	Sulfidic slate	Casing
	Slate	

Drill holes are younging towards south ↓

Stratigraphic section at Hall Bay area (outcrop 4 in Figure 1D)

Stromatolitic dolostone

Carbonate-magnetite

Slumped carbonate

Transitional facies

The transitional facies are absent in the drill holes

Strat column not to scale

Bridge Lake

B — B′

Depth (m)

PB12-32

PB12-33

BL12-37

EBL10-29

EBL10-27

EBL10-28

NGI10-31

Possible fault repetition

East Bridget Lake

North Galena Island

0 400 meters Approximate horizontal distance between the drill holes

N

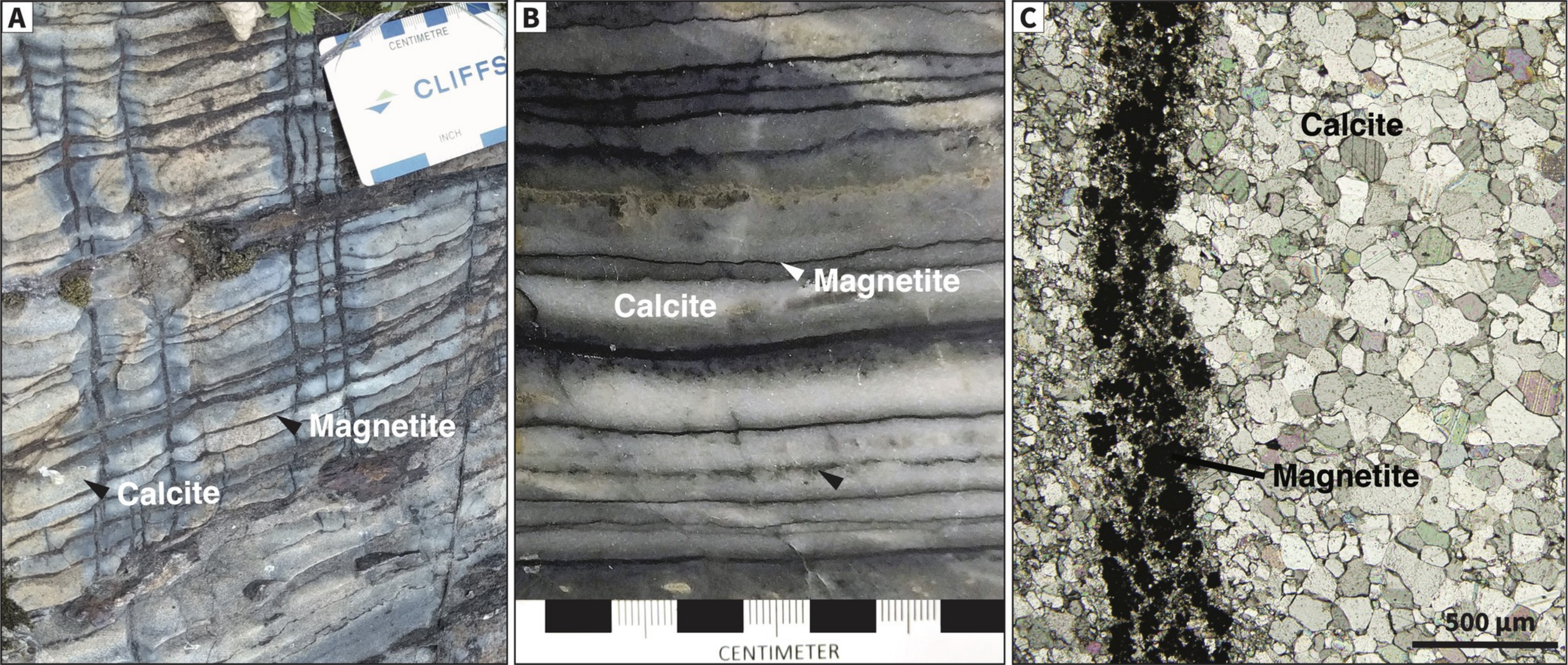
A
CENTIMETRE
CLIFFS
INCH
Magnetite
Calcite
B
Calcite
Magnetite
CENTIMETER
C
Calcite
Magnetite
500 µm

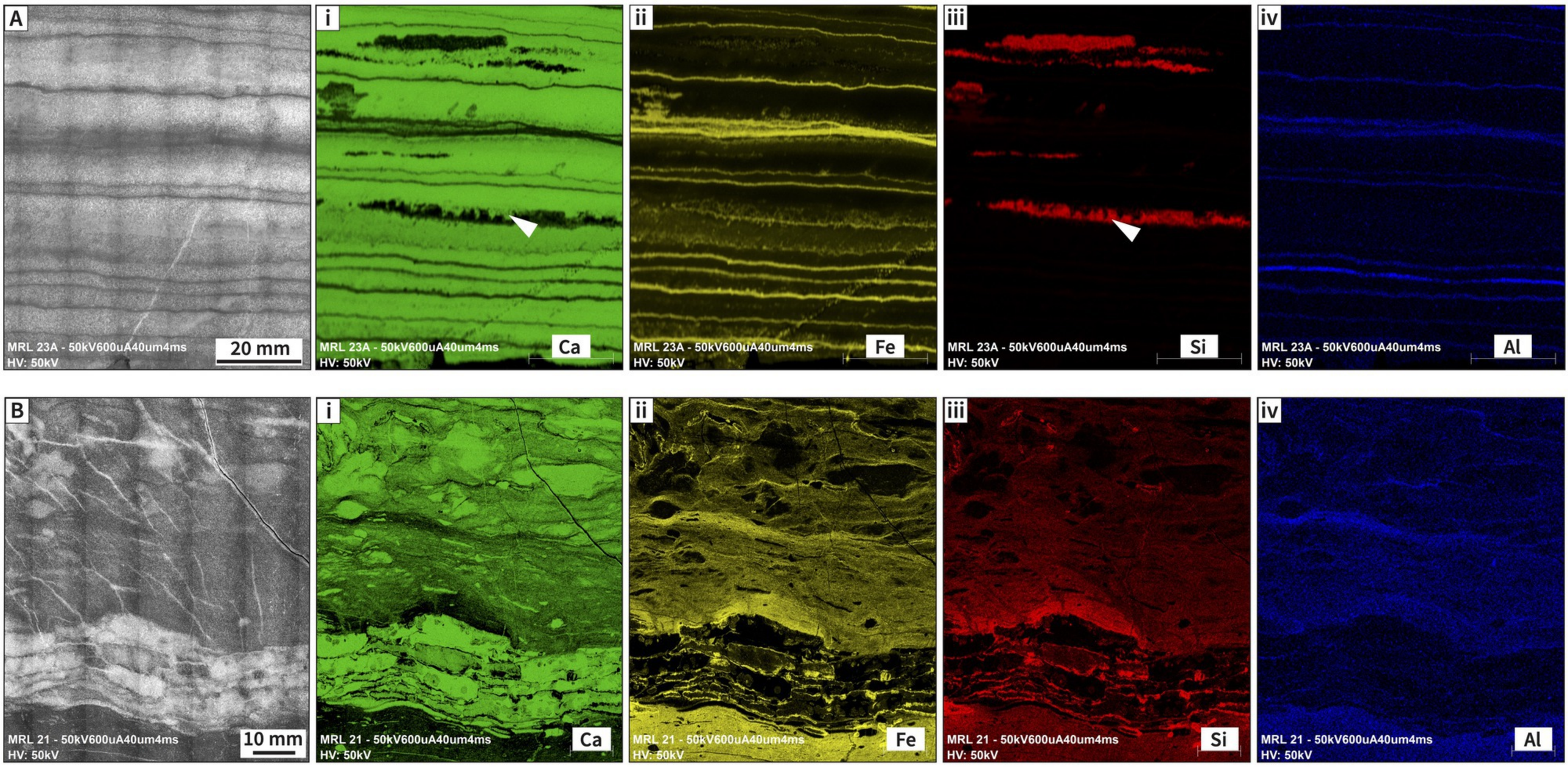
A
MRL 23A - 50kV600uA40um4ms
HV: 50kV
20 mm
i
MRL 23A - 50kV600uA40um4ms
HV: 50kV
Ca
ii
MRL 23A - 50kV600uA40um4ms
HV: 50kV
Fe
iii
MRL 23A - 50kV600uA40um4ms
HV: 50kV
Si
iv
MRL 23A - 50kV600uA40um4ms
HV: 50kV
Al
B
MRL 21 - 50kV600uA40um4ms
HV: 50kV
10 mm
i
MRL 21 - 50kV600uA40um4ms
HV: 50kV
Ca
ii
MRL 21 - 50kV600uA40um4ms
HV: 50kV
Fe
iii
MRL 21 - 50kV600uA40um4ms
HV: 50kV
Si
iv
MRL 21 - 50kV600uA40um4ms
HV: 50kV
Al

A

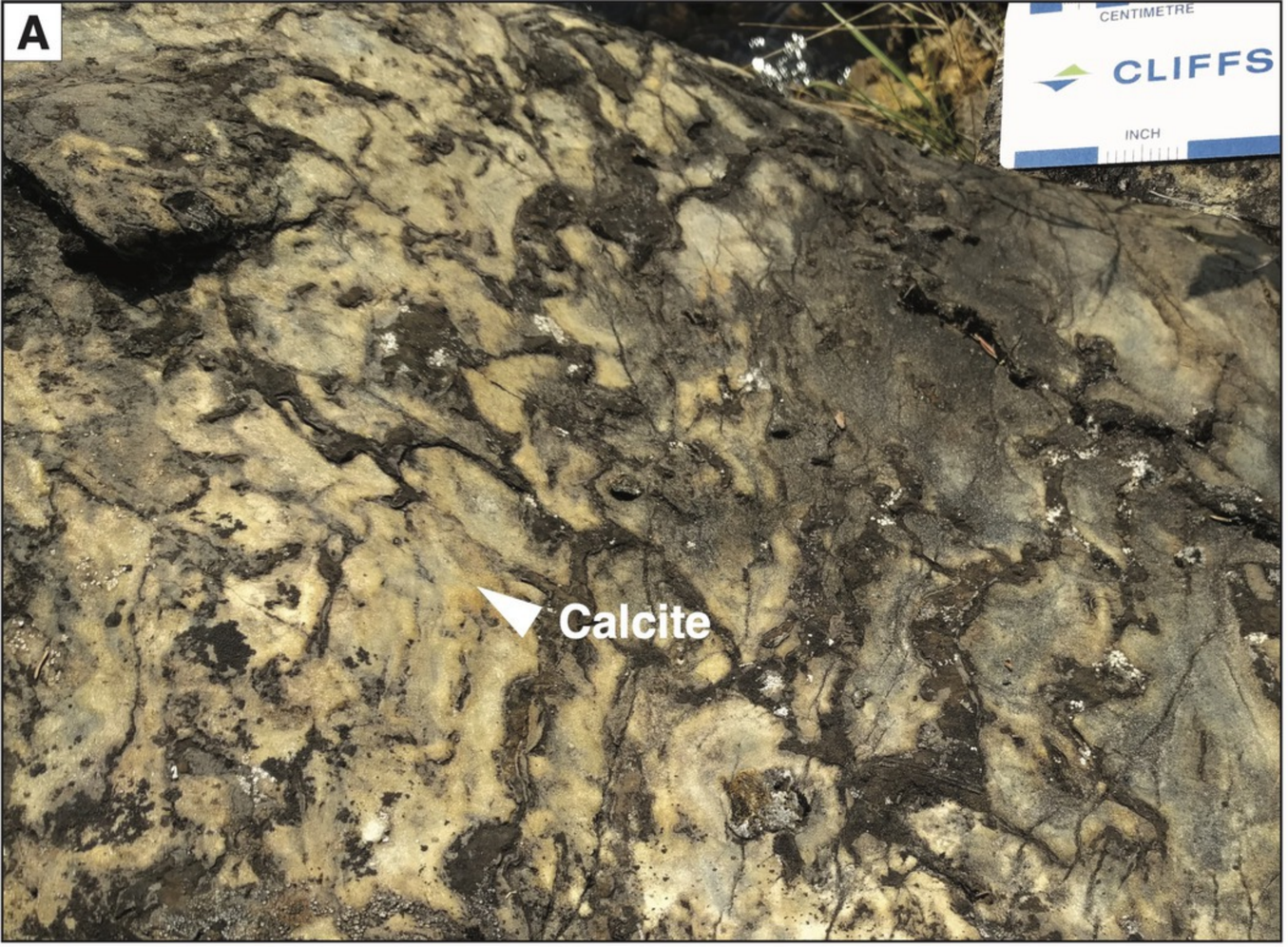
CENTIMETRE
CLIFFS
INCH
Calcite

B


Calcite
CENTIMETER

C

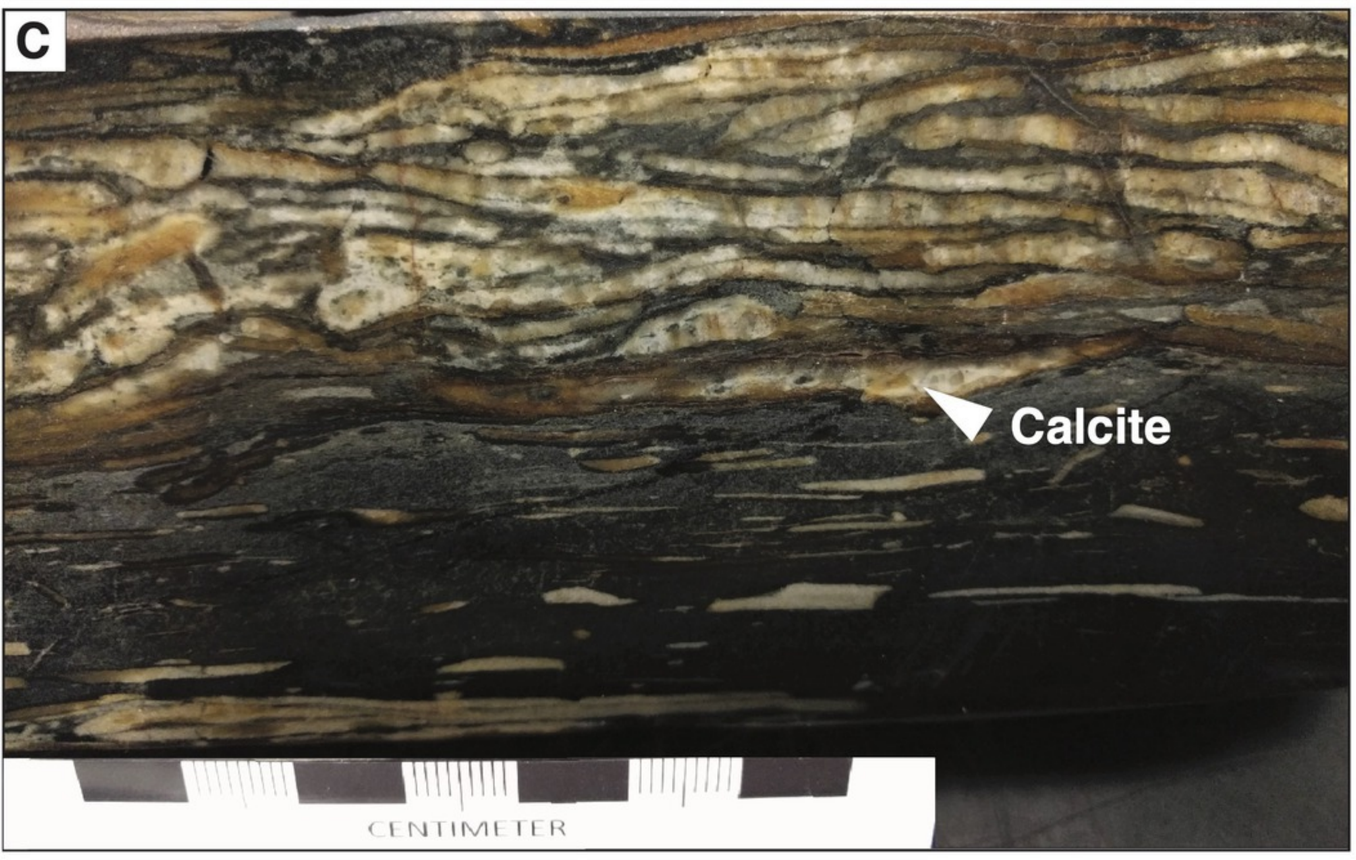
Calcite
CENTIMETER

D

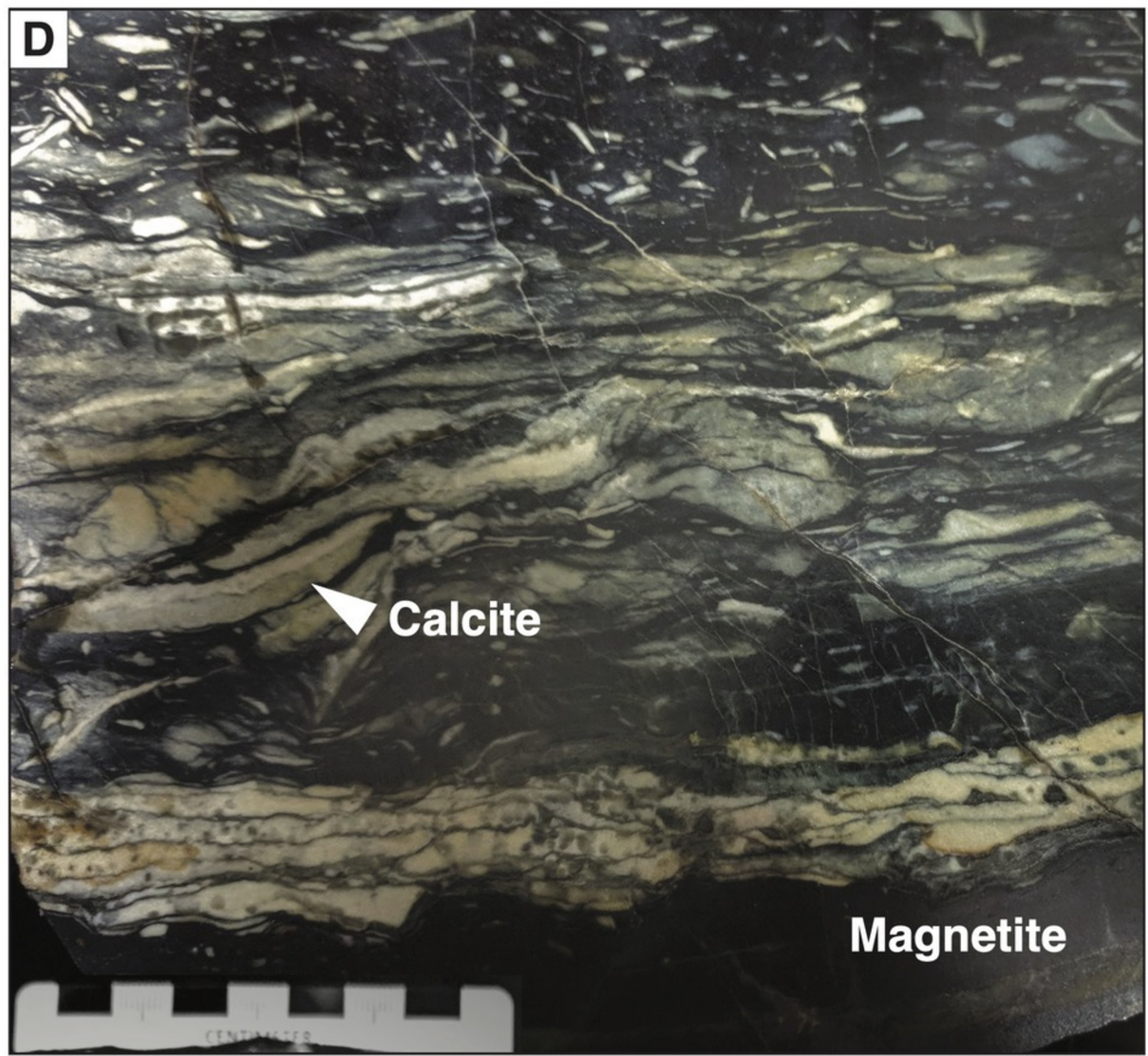
Calcite
Magnetite

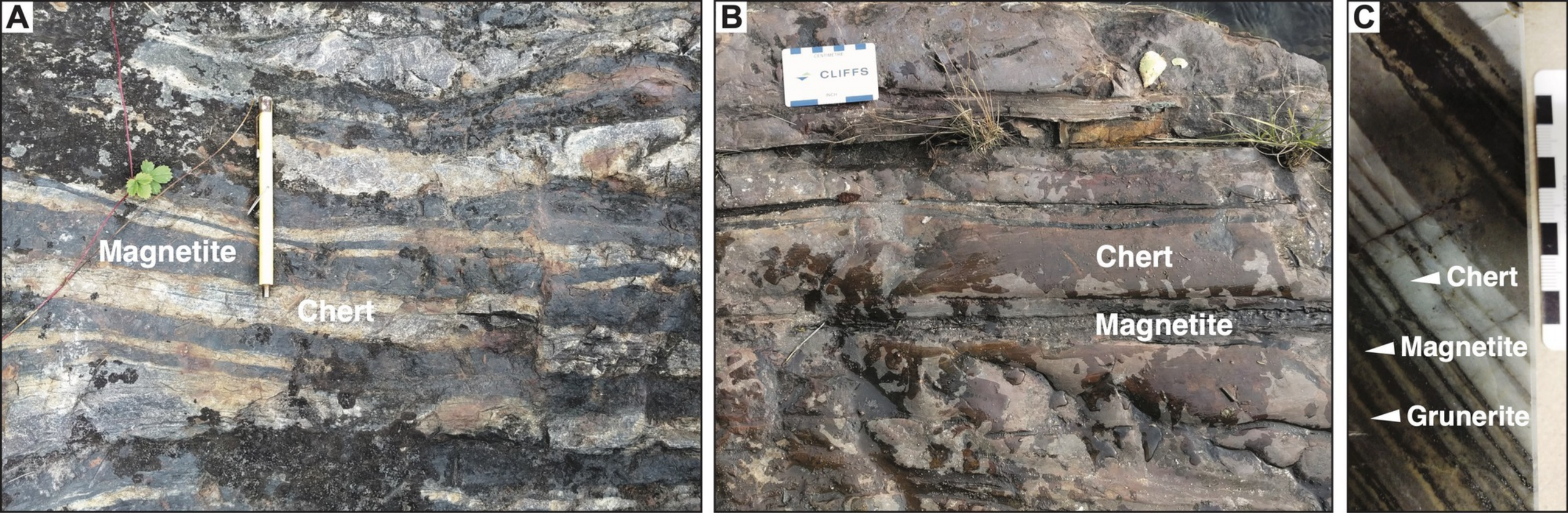
A
Magnetite
Chert
B
CLIFFS
Chert
Magnetite
C
Chert
Magnetite
Grunerite


A
Sulfidic slate
Chert
Oxide iron formation
CLIFFS

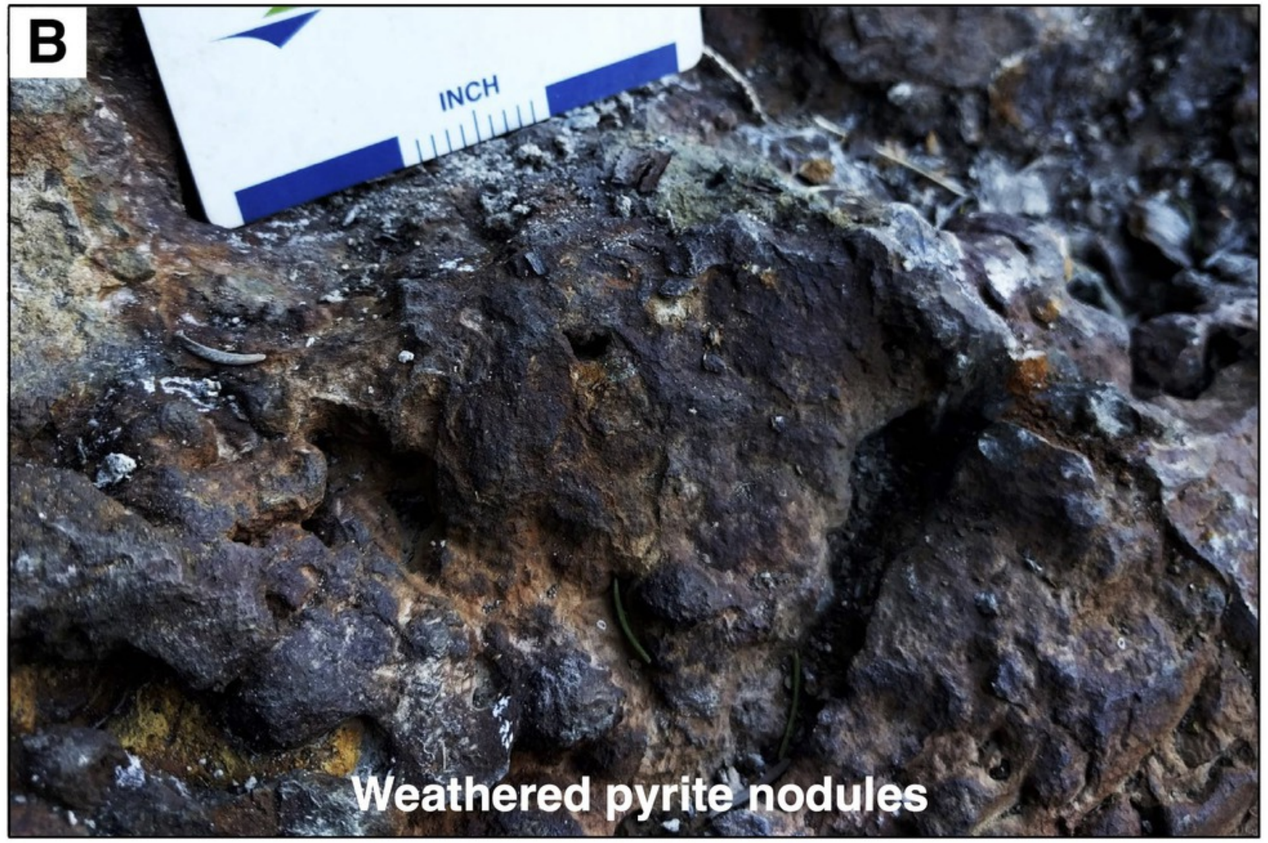
B
INCH
Weathered pyrite nodules

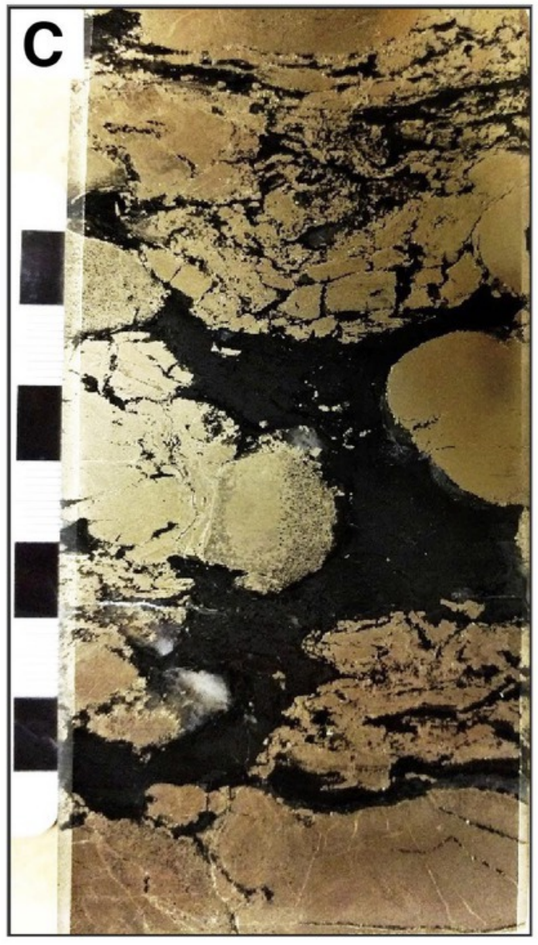
C

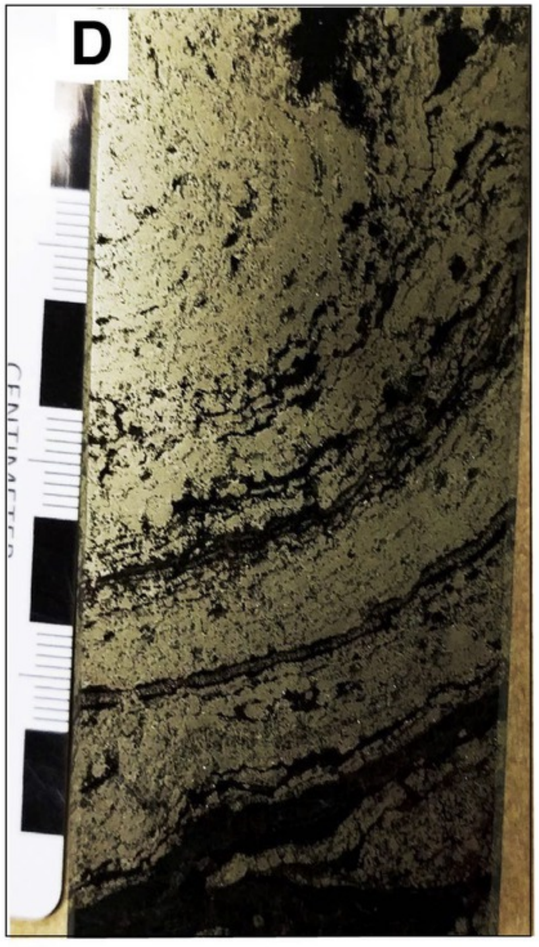
D

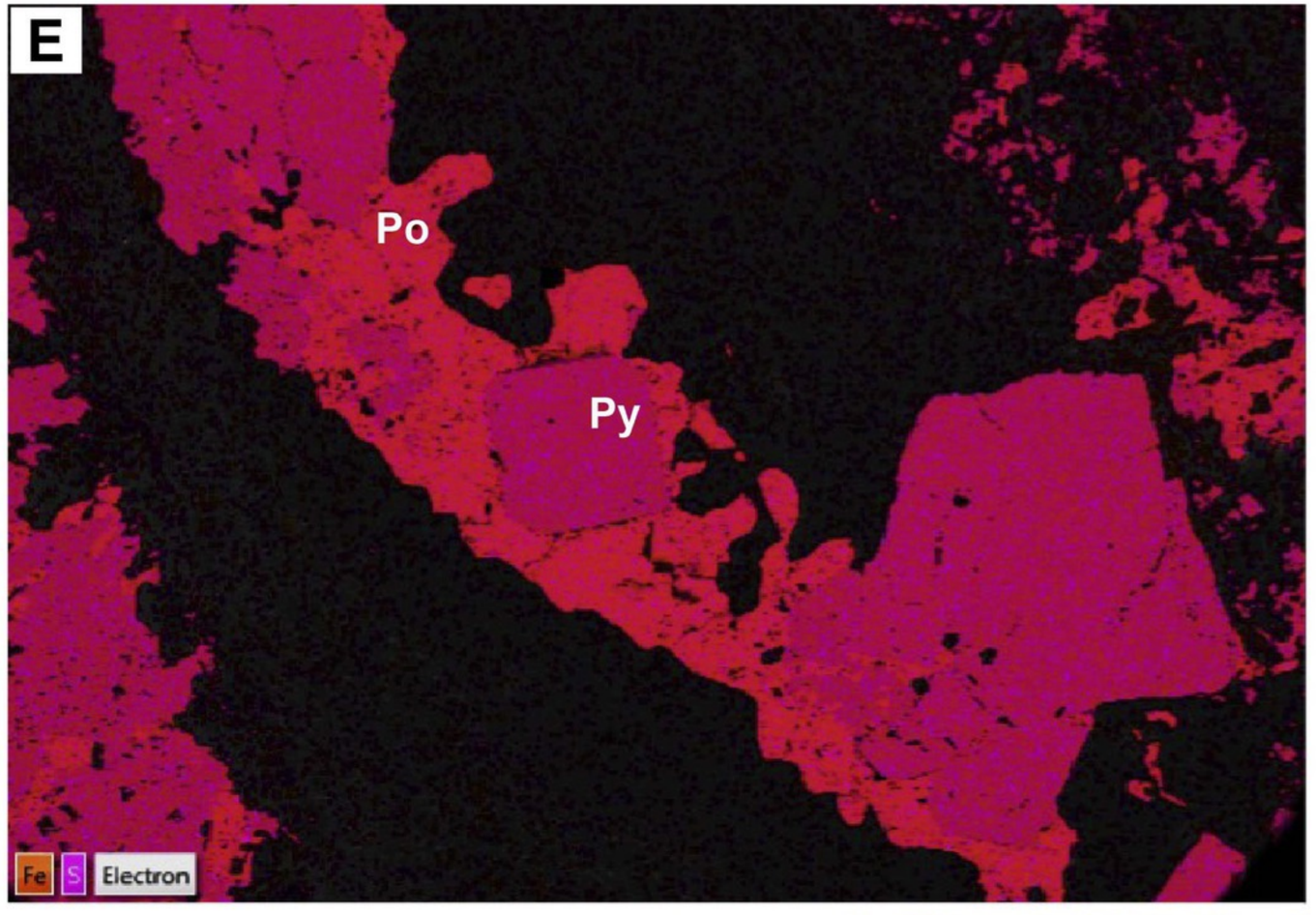
E
Po
Py
Fe
S
Electron

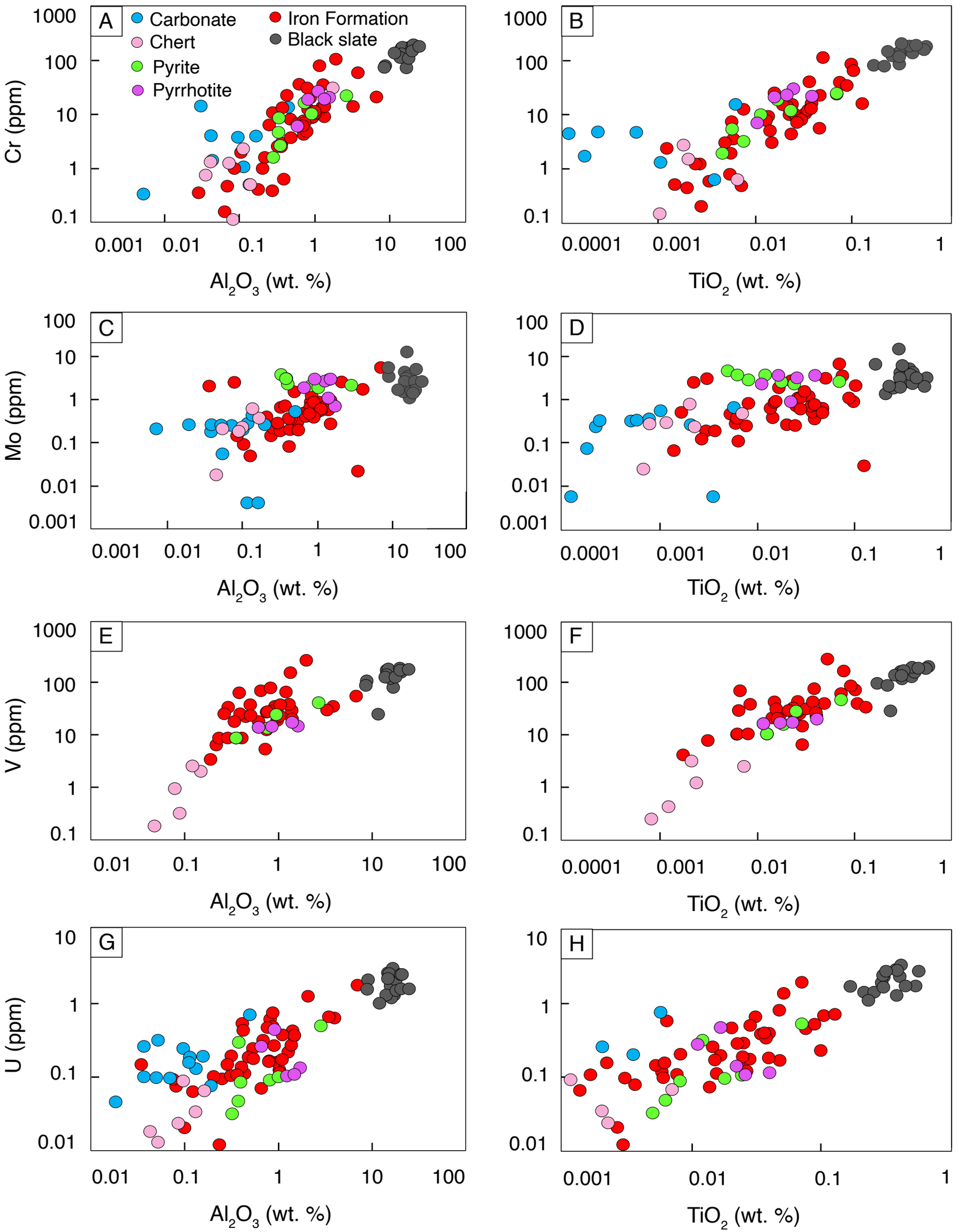
A
Carbonate
Chert
Pyrite
Pyrrhotite
Iron Formation
Black slate
Cr (ppm)
1000
100
10
1
0.1
0.001
0.01
0.1
1
10
100
Al2O3 (wt. %)
B
0.0001
0.001
0.01
0.1
1
TiO2 (wt. %)
C
Mo (ppm)
0.001
0.01
0.1
1
10
100
Al2O3 (wt. %)
D
0.0001
0.001
0.01
0.1
1
TiO2 (wt. %)
E
V (ppm)
0.1
1
10
100
1000
0.01
0.1
1
10
100
Al2O3 (wt. %)
F
0.0001
0.001
0.01
0.1
1
TiO2 (wt. %)
G
U (ppm)
0.01
0.1
1
10
0.01
0.1
1
10
100
Al2O3 (wt. %)
H
0.001
0.01
0.1
1
TiO2 (wt. %)

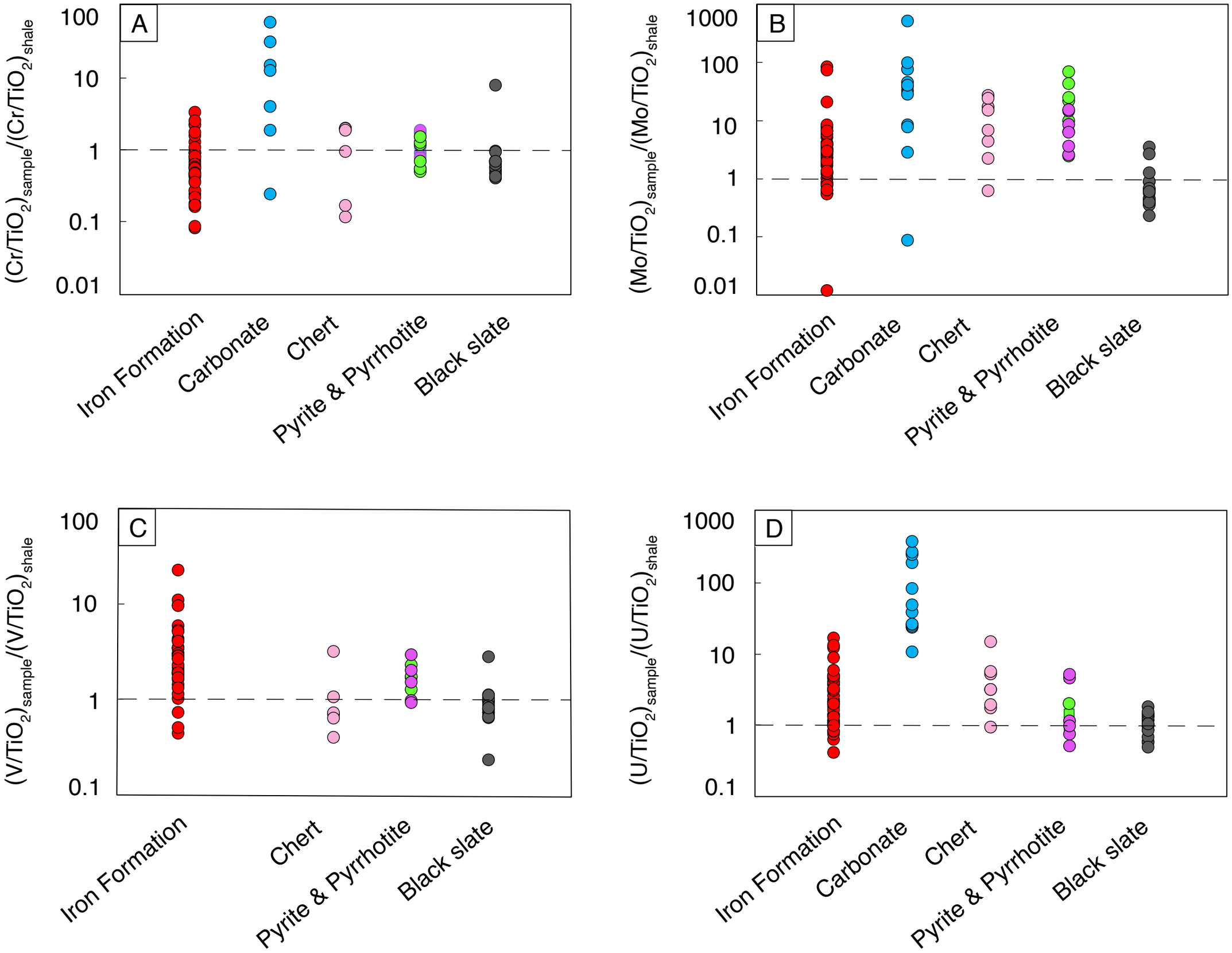
A
B
C
D
100
10
1
0.1
0.01
1000
$(Cr/TiO_2)_{sample}/(Cr/TiO_2)_{shale}$
$(Mo/TiO_2)_{sample}/(Mo/TiO_2)_{shale}$
$(V/TiO_2)_{sample}/(V/TiO_2)_{shale}$
$(U/TiO_2)_{sample}/(U/TiO_2)_{shale}$
Iron Formation
Carbonate
Chert
Pyrite & Pyrrhotite
Black slate

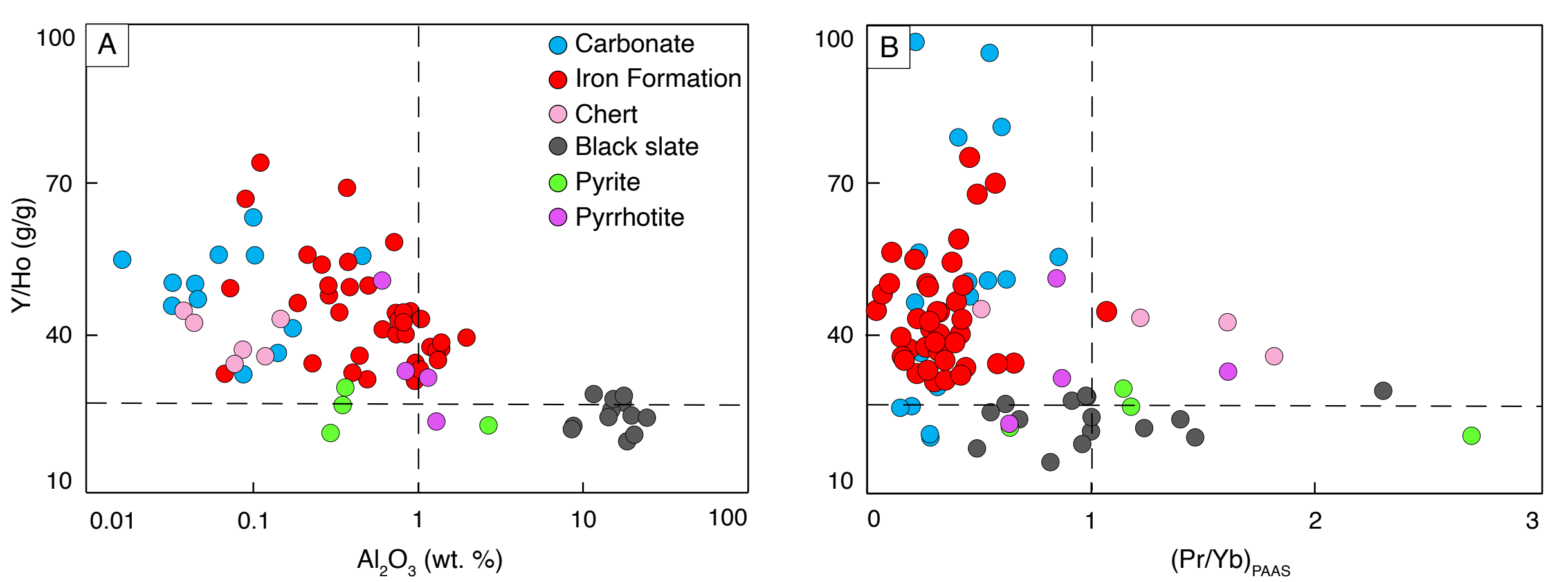
A
B
Carbonate
Iron Formation
Chert
Black slate
Pyrite
Pyrrhotite
Y/Ho (g/g)
100
70
40
10
0.01
0.1
1
10
100
Al2O3 (wt. %)
0
1
2
3
(Pr/Yb)PAAS

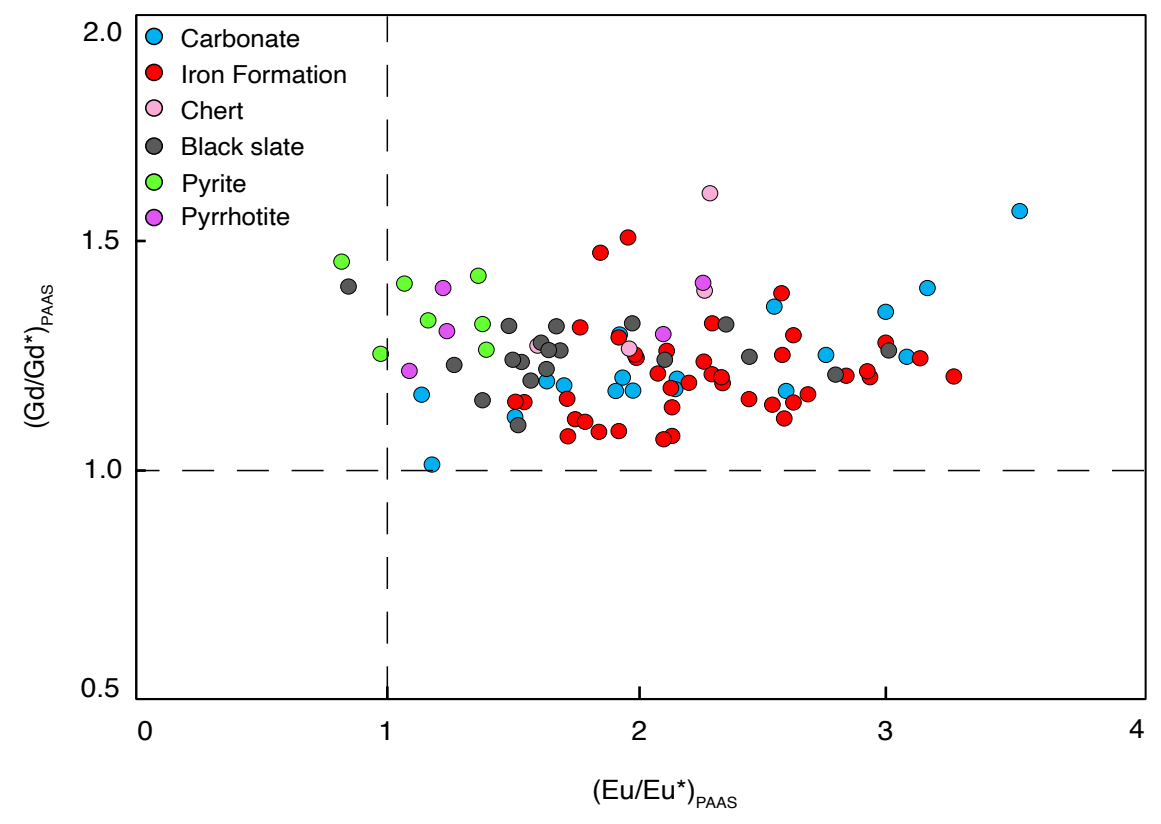
Carbonate
Iron Formation
Chert
Black slate
Pyrite
Pyrrhotite
2.0
1.5
1.0
0.5
0
1
2
3
4
(Gd/Gd*)PAAS
(Eu/Eu*)PAAS

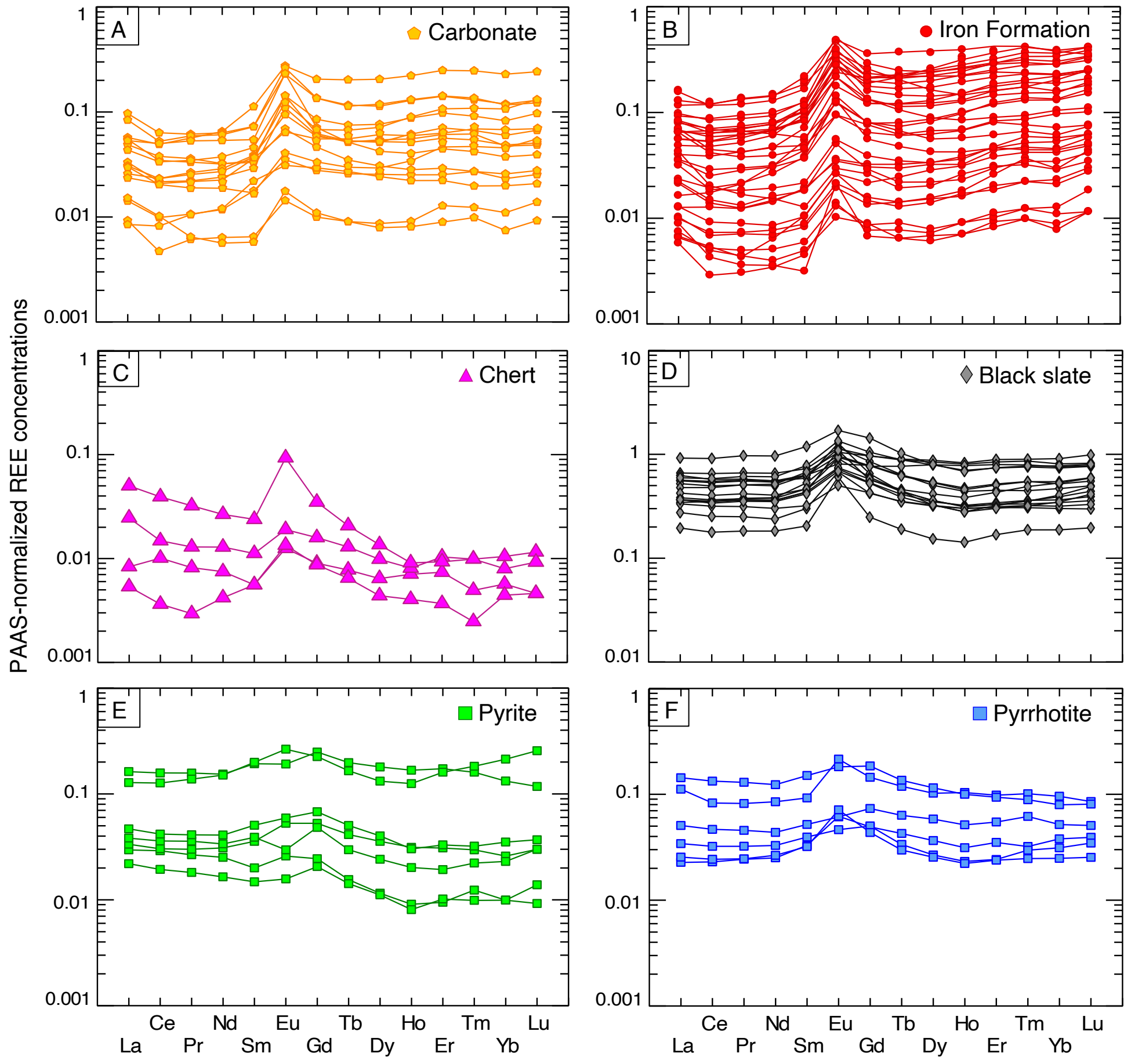
A
Carbonate
B
Iron Formation
C
Chert
D
Black slate
E
Pyrite
F
Pyrrhotite
PAAS-normalized REE concentrations
1
0.1
0.01
0.001
10
La
Ce
Pr
Nd
Sm
Eu
Gd
Tb
Dy
Ho
Er
Tm
Yb
Lu

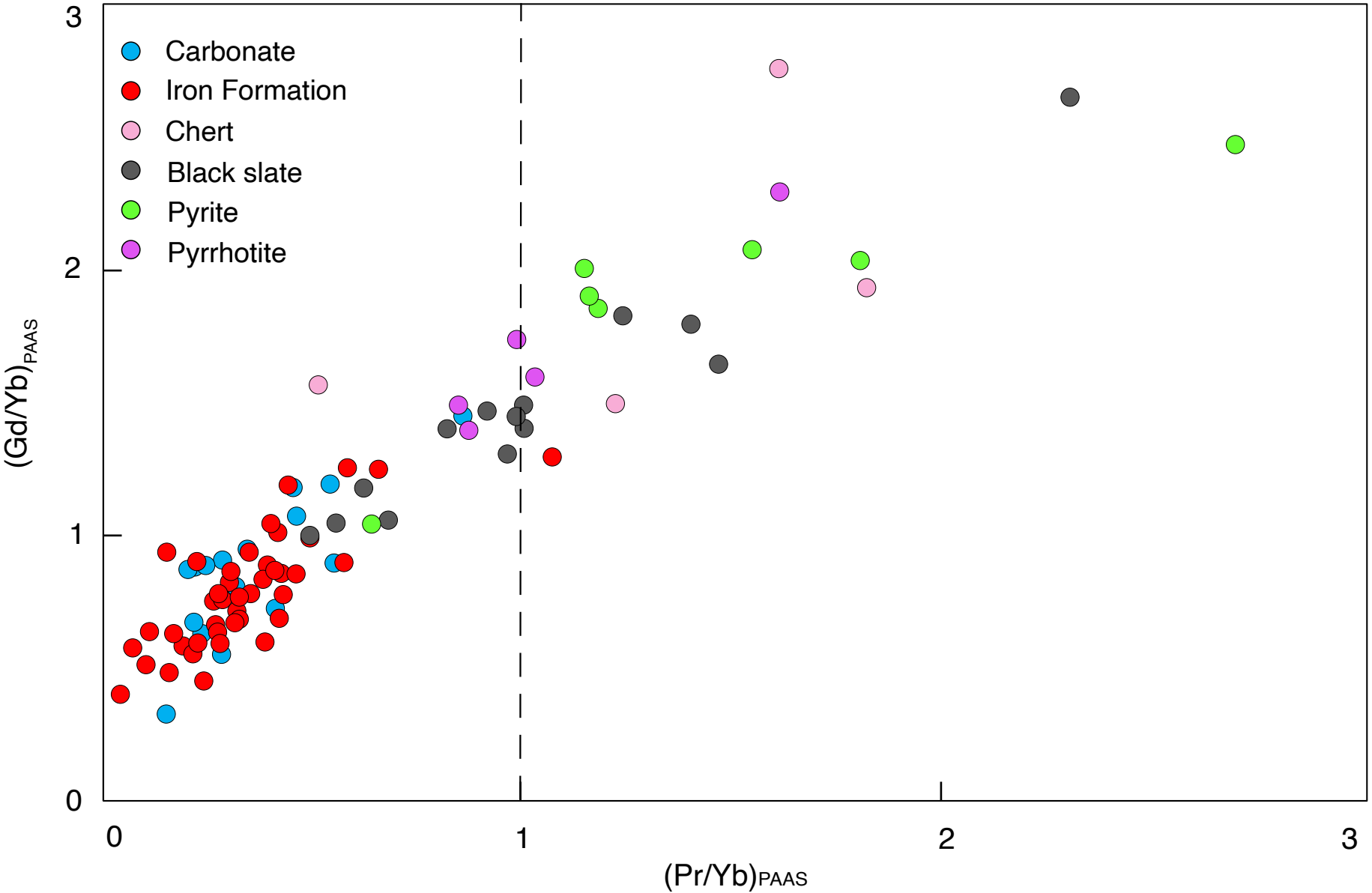
Carbonate
Iron Formation
Chert
Black slate
Pyrite
Pyrrhotite
(Gd/Yb)PAAS
(Pr/Yb)PAAS
0
1
2
3

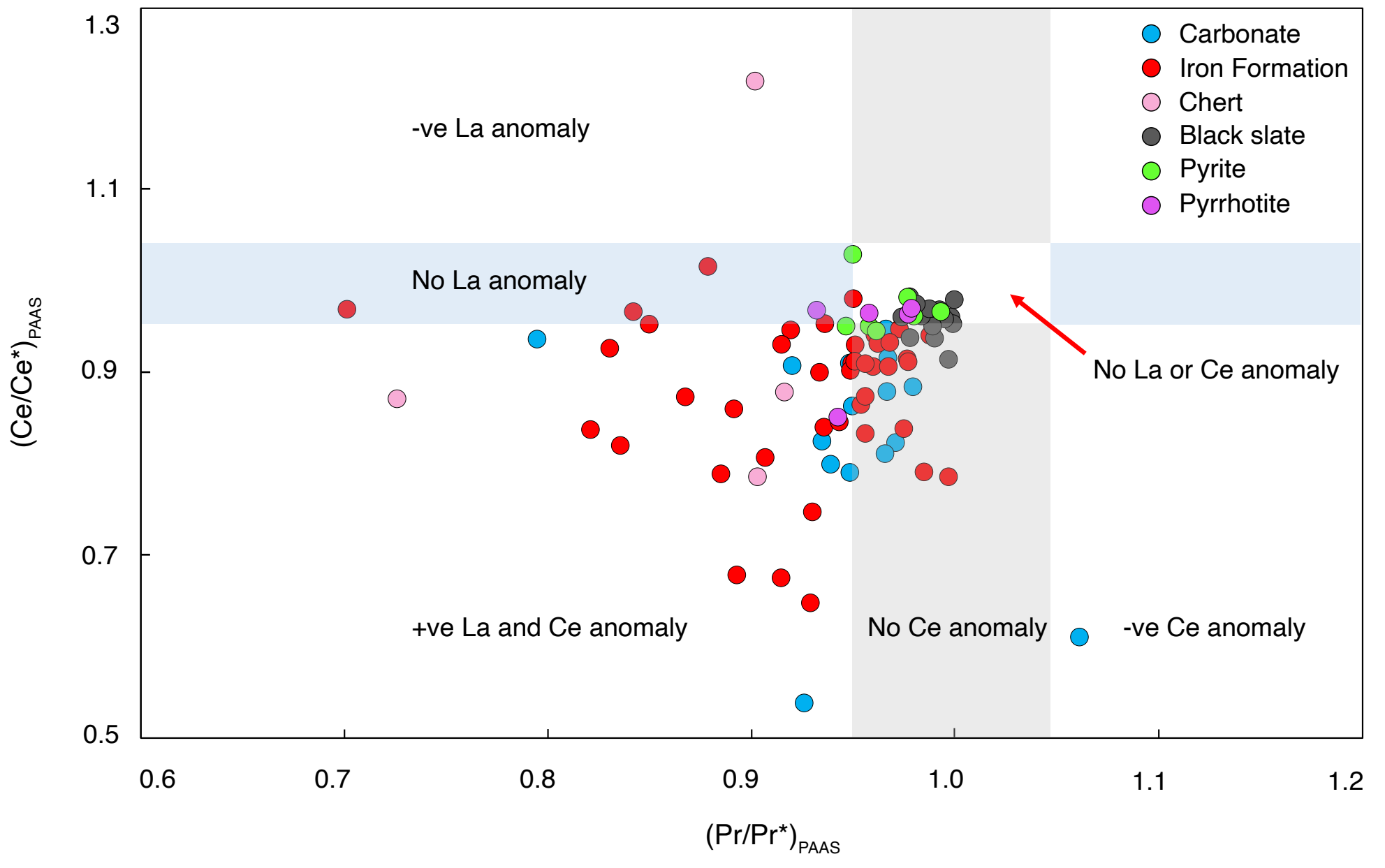
Carbonate
Iron Formation
Chert
Black slate
Pyrite
Pyrrhotite
-ve La anomaly
No La anomaly
No La or Ce anomaly
+ve La and Ce anomaly
No Ce anomaly
-ve Ce anomaly
1.3
1.1
0.9
0.7
0.5
0.6
0.7
0.8
0.9
1.0
1.1
1.2
(Ce/Ce*)PAAS
(Pr/Pr*)PAAS

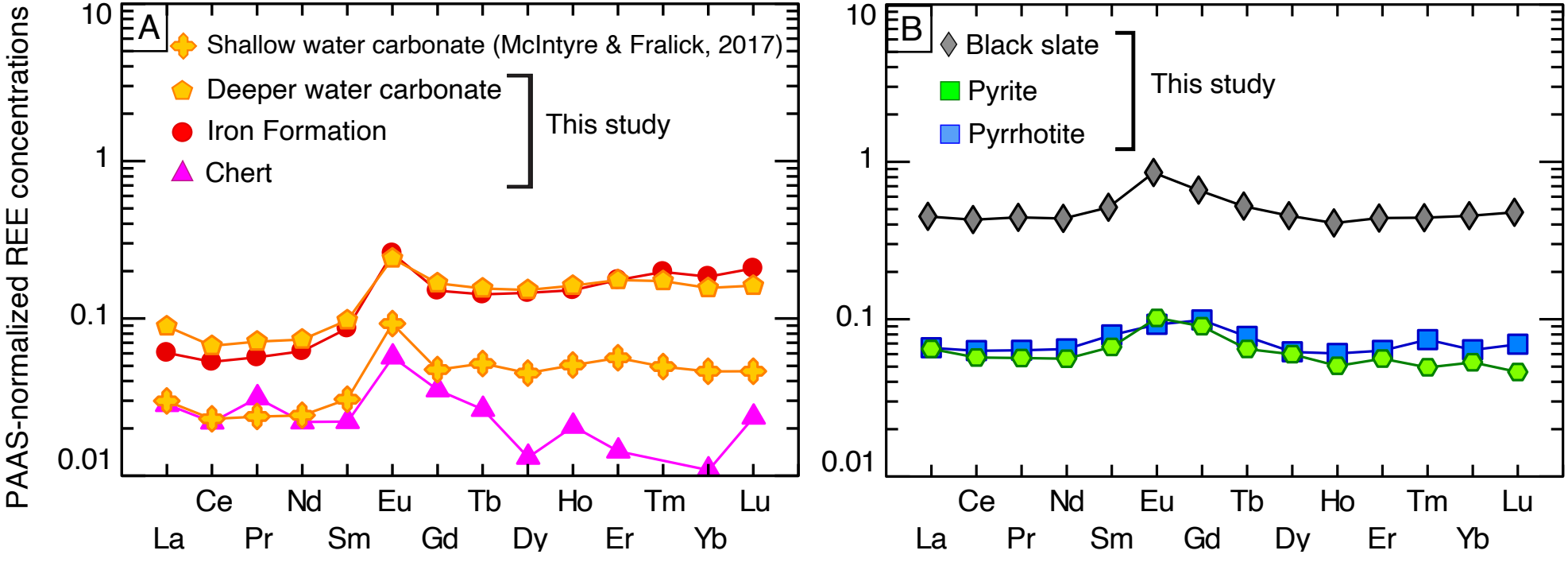
A
Shallow water carbonate (McIntyre & Fralick, 2017)
Deeper water carbonate
Iron Formation
Chert
This study
PAAS-normalized REE concentrations
10
1
0.1
0.01
La
Ce
Pr
Nd
Sm
Eu
Gd
Tb
Dy
Ho
Er
Tm
Yb
Lu
B
Black slate
Pyrite
Pyrrhotite
This study

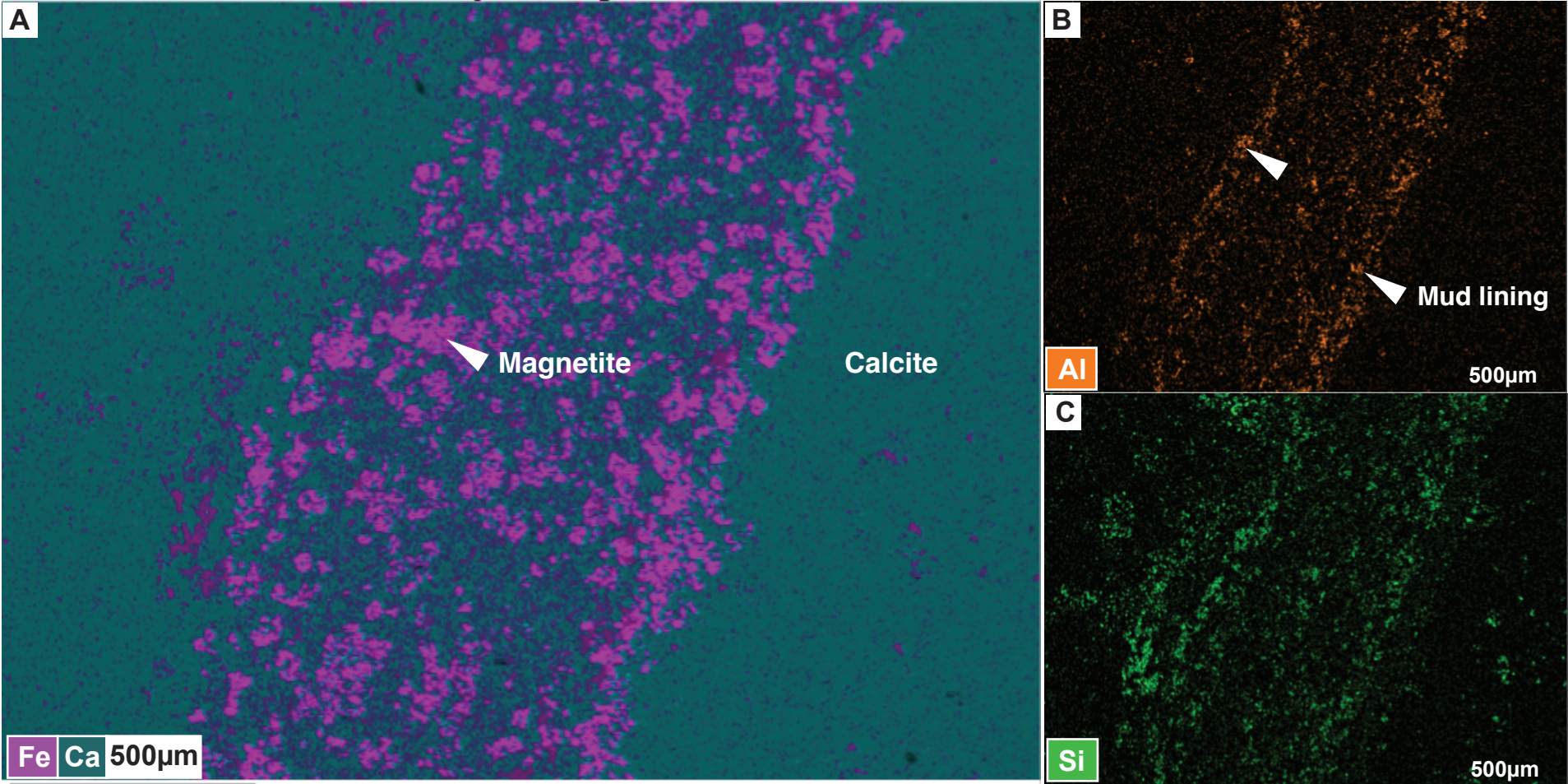
A
Magnetite
Calcite
Fe Ca 500µm
B
Mud lining
Al
500µm
C
Si
500µm